Chinese Journal of Chemical Engineering 95 (2026) 113–128

Contents lists available at ScienceDirect

Chinese Journal of Chemical Engineering

journal homepage: www.elsevier.com/locate/CJChE

Full Length Article

Dual Mo and Se vacancies in dual S-scheme heterojunction suppress charge recombination and boost redox capability for simultaneous removal of tetracycline and Cr(VI)

Pengfei Tian [1, 2], Yunan Shen [1, 2], Yuzhe Hua [1], Xiyu Zou [1], Guangmin Ren [1, *], Qingjie Guo [1], Hongjing Tian [1, 2, *]

[1] College of Chemical Engineering, Qingdao University of Science & Technology, Qingdao 266042, China
[2] State Key Laboratory of Advanced Optical Polymer and Manufacturing Technology, Yantai 264000, China

ARTICLE INFO

Article history:
Received 8 October 2025
Received in revised form
19 January 2026
Accepted 23 January 2026
Available online 16 February 2026

Keywords:
Dual vacancies
Dual S-scheme heterojunction
Rapid charge transfer
Redox capability
Bi-directional promotion effects

ABSTRACT

Mo vacancy (V_{Mo}) and Se vacancy (V_{Se}) are doped into Bi_2MoO_6 (BMO) and ZnSe, respectively, while they are mechanically ground and mixed to fabricate the dual S-scheme heterojunction. The lattice distortion is observed at the interface between V_{Mo}-BMO and V_{Se}-ZnSe/CdSe (V_{Se}-ZCS) while XPS results confirm the construction of the dual S-scheme heterojunction V_{Mo}-BMO/V_{Se}-ZCS (V_{Mo+Se}-BZCS). DFT simulation demonstrate that the doping of V_{Mo} and V_{Se} lead to more electrons transferring spontaneously through the heterojunction interfaces and promote the IEF strength accordingly. Both *in-situ* XPS and fs-TAS characterization prove the presence of a fast photoinduced charge transfer pathway from V_{Mo}-BMO to V_{Se}-ZnSe under LED light irradiation. V_{Mo} and V_{Se} function as the holes trapping center in V_{Mo}-BMO and the electron trapping center in V_{Se}-ZCS, respectively, thereby effectively suppressing the electron-hole recombination, which enhances the redox capability of V_{Mo+Se}-BZCS together with the fast charge transferring. During the photocatalytic degradation experiments for the wastewater containing both tetracycline (TC) and Cr(VI), both the TC and the Cr(VI) degradation efficiency of V_{Mo+Se}-BZCS are competitive under either LED or xenon lamp irradiation in comparison with some reported catalysts. Dual doping of V_{Mo} and V_{Se} were testified to amplify the bi-directional promotion effects (BPEs) between TC and Cr(VI).
© 2026 The Chemical Industry and Engineering Society of China, and Chemical Industry Press Co., Ltd. All rights are reserved, including those for text and data mining, AI training, and similar technologies.

1. Introduction

Human activities have been proved to exacerbate the combined pollution emission of organic pollutants and heavy metals, whereas traditional degradation managements targeted primarily the single pollutants [1,2]. Tetracycline (TC) is a typical broad-spectrum antibiotic and extensively utilized in industrial production due to its outstanding antibacterial performance [3]. Chromium is the most common of the heavy metal contaminants while hexavalent chromium (Cr(VI)) is more toxic than Cr(III) owing to its high oxidizing potential [4]. Both TC and Cr(VI) are highly stable and the electron-rich functional groups of TC easily combine with Cr(VI) to generate medical metal complexes, which are more inclined to bioaccumulate and biomagnify through the food chain. Eventually, industrial or domestic wastewater containing TC and Cr(VI) amplify risks to ecosystems and human health. Therefore, there is an urgent need to develop an efficient wastewater treatment for simultaneous removal of TC and Cr(VI) [5].

Photocatalytic degradation can utilize the photoinduced electrons and holes in semiconductor catalysts to degrade various pollutants efficiently under mild conditions [6–8]. As a member of the Aurivillius-phase family, bismuth molybdate (Bi_2MoO_6, BMO) consisting of alternating perovskite-like $[MoO_4]^{2-}$ layers and fluorite-like $[Bi_2O_2]^{2+}$ layers was considered to be a promising candidate of photocatalysis because of its unique perovskite-type layered structure and wide range of light absorption [9–11]. However, such intrinsic limitations of pristine BMO as the deficiency of active sites for surface reactions and the swift recombination of charge carriers severely restricts its photocatalytic activity [12,13]. ZnSe is regarded as a promising

* Corresponding authors.
E-mail addresses: 17568022691@163.com (G. Ren), hj_tian@qust.edu.cn (H. Tian).

https://doi.org/10.1016/j.cjche.2026.01.011
1004-9541/© 2026 The Chemical Industry and Engineering Society of China, and Chemical Industry Press Co., Ltd. All rights are reserved, including those for text and data mining, AI training, and similar technologies.

selection to combine with BMO to create S-scheme heterojunction owing to its narrow band gap and high reduction potential [14,15]. The S-scheme heterojunction alleviates the electron transfer from the oxidized semiconductor to the reduced semiconductor, leading to the effective separation of the photoinduced electrons and holes, eventually rendering itself an outstanding redox activity [16–18].

Vacancy engineering strategy can introduce new defect states in the band gap and subtly modulate the band gap of the photocatalyst [19]. The regulated electronic structure of photocatalyst was beneficial to reinforce the migration and separation of photoexcited carriers [20,21]. Additionally, anion defects and cation vacancies commonly act as electron trapping centers (electron acceptors) and hole trapping centers (electron donors), respectively, which enhances the mobility of photoinduced electrons and holes [22,23]. Zhao *et al.* [24] developed the defective $ZnIn_2S_4$ rich in dual Zn and In cation vacancies and reported that the defect states accelerated the transfer of photoelectrons from VB to CB, thereby improving the carrier separation efficiency. However, most of the dual-vacancy engineering strategies doped dual metal or nonmetal vacancies into the reduction photocatalyst (RP) or the oxidation photocatalyst (OP) alone in the S-scheme heterojunction. Such vacancies were difficult to be precisely localized and confined in the heterojunction, probably rendering them mutually restrictive, even forming carrier recombination centers and weakening the redox activity [25]. Huang *et al.*[26] fabricated the $BiVO_4$ photoanodes with dual V and O vacancies and proved that excessive V vacancies significantly restricted the action of O vacancies and caused the formation of carrier recombination. In this context, the precise introduction of anionic and cationic vacancies into RP and OP of the S-scheme heterojunctions create the electron trapping and the hole trapping centers in RP and OP, respectively. Furthermore, the resulting directionally coordinated internal electric field (IEF) in the heterojunction suppress the electron-hole recombination and optimize the photoinduced charge transfer pathway. Additionally, the bidirectional promotion effects (BPEs) were reported for the simultaneous photocatalytic removal of Cr(VI) and tetracycline hydrochloride (TCH) with $SnNb_2O_6/CuInS_2$ S-scheme heterojunction as the catalyst. The directionally coordinated IEF was expected to generate a "cascade amplification" effect on the BPEs.

Herein, both deep eutectic solvent impregnation and ion exchange methods were employed to construct a dual-vacancy engineered S-scheme heterojunction with Mo vacancies (V_{Mo}) and Se vacancies (V_{Se}) (V_{Mo+Se}-BZCS) [14,15]. During the ion exchange process, both the structural distortion of ZnSe and the formation of CdSe on the surfaces of ZnSe occurred because the solubility product (K_{sp}) of CdSe ($10^{-35.2}$) was much lower than ZnSe ($10^{-25.4}$), greatly facilitating the generation of V_{Se} [27]. The simultaneous photocatalytic degradation of tetracycline (TC) and reduction of Cr(VI) in wastewater, with V_{Mo+Se}-BZCS as the photocatalyst, were carried out under low-cost light emitting diodes (LED) visible light irradiation (λ = 420–780 nm). LED panel exhibited the higher energy efficiency, longer life expectancy, larger color gamut, and more compact design than the conventional xenon lamp. The effects of dual V_{Mo} and V_{Se} on the electron-hole separation and the charge transfer pathway in V_{Mo+Se}-BZCS during the simultaneous removal of TC and Cr(VI), as well as on the amplification of BPEs between TC and Cr(VI), were investigated. Both femtosecond transient absorption

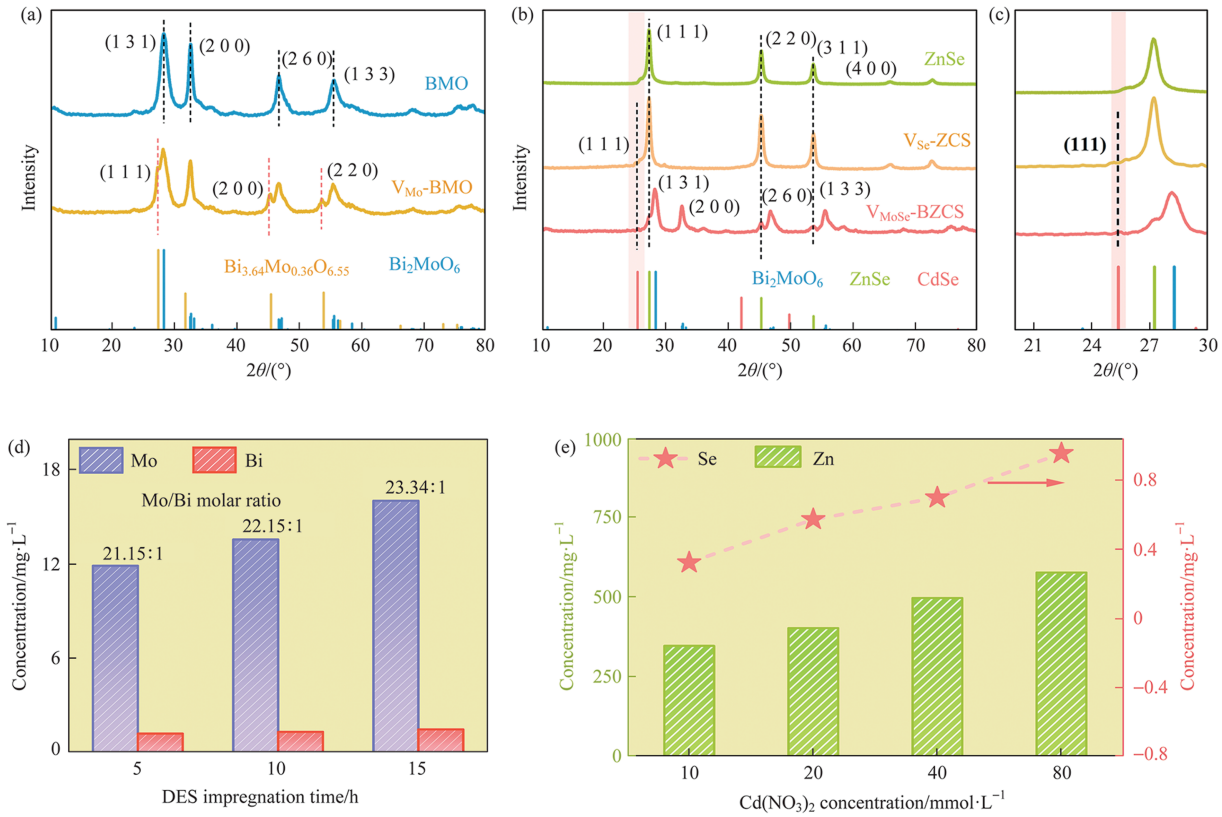


Fig. 1. XRD patterns of (a) BMO and V_{Mo}-BMO, (b-c) ZnSe, V_{Se}-ZCS, and V_{Mo+Se}-BZCS, (d) Bi and Mo ion concentration of the filtrate after the treatment of BMO with different DES impregnation time, (e) Zn and Se ion concentration of the filtrate after the treatment of ZnSe with different $Cd(NO_3)_2$ concentration, (f) HRTEM image of V_{Mo}-BMO, (g) the intensity profile of Bi and Mo atom in the green and yellow box in the enlarged image in (f), (h)-(i) HRTEM image of V_{Se}-ZCS.

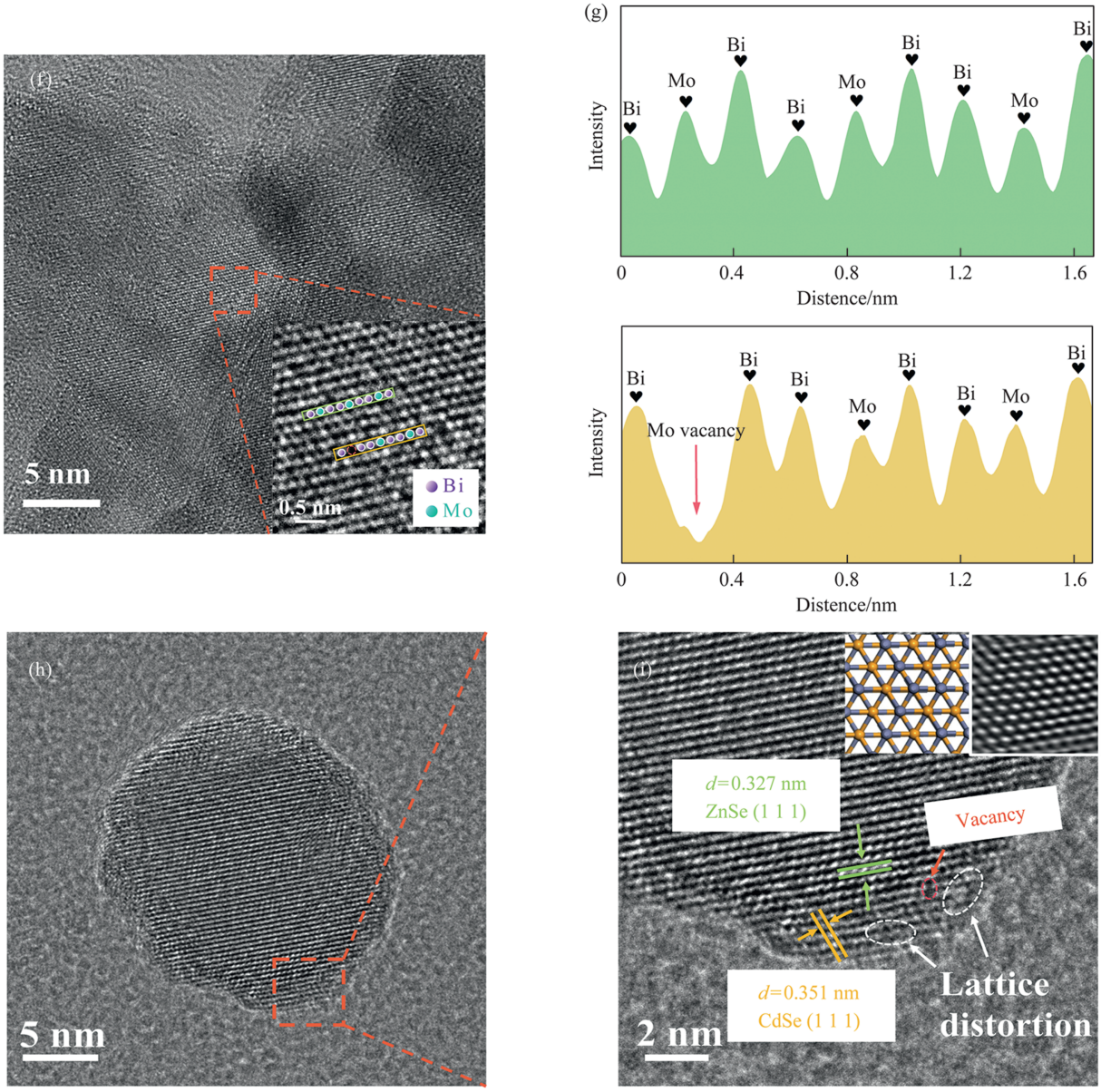


Fig. 1. (*continued*).

spectroscopy (fs-TAS) characterization and DFT simulation results elucidated the photocatalytic degradation mechanism of TC and Cr(VI) for the dual S-scheme heterojunction. This work offered a promising avenue for enhancing the interfacial charge transfer in the S-scheme heterojunction and improving its redox ability.

2. Experimental

2.1. Chemicals

Bismuth nitrate pentahydrate ($Bi(NO_3)_3·5H_2O$, AR, ≥99.7%), zinc nitrate hexahydrate ($Zn(NO_3)_2·6H_2O$, AR, ≥99.0%), ethylene glycol ($C_2H_6O_2$), ethanol (C_2H_5OH, AR), *p*-benzoquinone (BQ, $C_6H_4O_2$, CP, 98%), isopropanol (IPA, C_3H_8O, AR, ≥99.7%), ethylenediamine tetra acetic acid disodium salt dihydrate (EDTA-Na,$C_{10}H_{14}N_2Na_2O_8·2H_2O$, AR, ≥99.0%), anhydrous sodium sulfate (Na_2SO_4, AR, ≥99.0%), anhydrous sodium carbonate (Na_2CO_3, AR, ≥99.0%), nitric acid (HNO_3, 65% to 68%), potassium dichromate ($K_2Cr_2O_7$, GR, 99.8%), 1, 5-diphenylcarbazide ($C_{13}H_{14}N_4O$, AR) were obtained from Sinopharm Chemical Reagent Co., LTD. Anhydrous sodium molybdate (Na_2MoO_4, AR, ≥99.7%), sodium borohydride ($NaBH_4$, 96%), cadmium nitrate tetrahydrate ($Cd(NO_3)_2·4H_2O$, AR, ≥99.0%) were bought from McLean Biochemical Co., Ltd. Selenium powder (Se) and Nafion perfluorinated resin solution (Polymer Content:5.0% to 5.4%, Water Content:42% to 48%) were purchased from Aladdin Reagent Co., Ltd. Tetracycline (TC, $C_{22}H_{24}N_2O_8$, CP, ≥98.0%) was obtained from Merck Chemicals (Shanghai) Co., Ltd.

2.2. Preparation of V_{Mo+Se}-BZCS, V_{Mo}-BZCS and V_{Se}-BZCS

V_{Mo}-BMO and V_{Se}-ZCS were firstly prepared according to the method in Supplementary Material. They were mixed with the mass fraction of V_{Se}-ZCS at 5%, 15%, 20%, 25%, 30%, and 50%, respectively, and mechanically ground for 30 min. The related preparation scheme was illustrated as Fig. S1. BMO and ZnSe were

ground for 1 h at a mass ratio of 3:1 to obtain BMO/ZnSe. ZCS was prepared according to the method in Supplementary Material. BMO and ZCS were ground for 1 h at a mass ratio of 3:1, and the resulting sample was labeled as BZCS. V_{Mo}-BMO and ZCS were ground for 1 h at a mass ratio of 3:1, and the resulting sample was designated as V_{Mo}-BZCS. BMO and V_{Se}-ZCS were thoroughly ground for 1 h at a mass ratio of 3:1, and the resulting sample was designated as V_{Se}-BZCS.

2.3. Photocatalytic degradation experiment

Photocatalytic degradation experiments were performed using a 40 W LED lamp as the visible light source (wavelength range: 400–830 nm; lamp diameter: 10 cm). First, 50 mg of catalyst was added into 100 ml of TC (40 mg·L^{-1}) and Cr(VI) (40 mg·L^{-1}) solution. The mixtures were stirred in a dark environment for 30 min to achieve the adsorption equilibrium of photocatalysts. Subsequently, the solution was irradiated under LED for 120 min while the temperature was controlled at 25 °C using the circulating water. 1 ml of aliquots were collected every 15 min and filtered by the membrane with the pore size of 0.22 μm. The concentration of TC and Cr(VI) was determined by measuring the absorbance at 357 nm and 540 nm, respectively, using an ultraviolet-visible spectrophotometer, while Cr(VI) was quantified by the 1,5-diphenylcarbazide (DPC) colorimetric method. After obtaining the spent catalysts by centrifugation, they were washed three times with absolute ethanol and deionized water, respectively, dried at 60 °C, and weighed. The volume of the solution in the degradation system was adjusted to maintain the catalyst loading constant at 0.5 g L^{-1} for all the degradations. TC and Cr(VI) degradation efficiency were calculated as described in Supplementary Material.

Both characterization and DFT computational details were outlined in the Supplementary Material. *Escherichia coli* growth inhibition experiment method was also presented in Supplementary Material to evaluate the biotoxicity of the degradation solutions after the degradation tests.

3. Results and Discussion

3.1. Doping of V_{Mo} and V_{Se} in the catalyst

Both the XRD patterns of BMO before and after DES impregnation (Fig. 1(a)) showed that the diffraction peaks of BMO aligned well with the standard pattern of Bi_2MoO_6 (JCPDS 72-1524) [28]. Meanwhile, the V_{Mo}-BMO sample exhibited additional peaks ascribed to $Bi_{3.64}Mo_{0.36}O_{6.55}$ (JCPDS 43-0446), indicating that DES impregnation induced Mo leaching and V_{Mo} formation in BMO [25]. Fig. 1(b) and (c) provided a comparison of the XRD patterns of ZnSe, V_{Se}-ZCS, and V_{Mo+Se}-BZCS. V_{Se}-ZCS displayed a weak diffraction peak at 25.36°, which was assigned to the (1 1 1) crystal plane of CdSe (JCPDS 88-2346). The same peak was also observed in the pattern of V_{Mo+Se}-BZCS, confirming that V_{Mo+Se}-BZCS contained BMO, ZnSe, and CdSe. Both the Mo and Bi concentrations (Fig. 1(d); Table S1) were detected in the filtrate by ICP-OES characterization after the impregnation of BMO by DES. When the impregnation time increased from 5 h to 15 h, the Mo/Bi molar ratio changed from 21.15:1 to 23.34:1, confirming that DES impregnation preferentially broke Mo–O bonds and produced V_{Mo} in BMO. It was demonstrated that the concentration of V_{Mo} could be controlled by adjusting the DES impregnation time. Both the concentrations of Zn and Se (Fig. 1(e); Table S2) in the electrolyte solution, after the replacing of Zn^{2+} by Cd^{2+} from $Cd(NO_3)_2$ solution, were determined as well. When the $Cd(NO_3)_2$ concentration increased from 10 mmol·L^{-1} to 80 mmol·L^{-1}, the molar amount of Zn^{2+} in the electrolyte solution increased from 346.87 mg·L^{-1} to 576.42 mg·L^{-1}. The great difference between the K_{sp} of CdSe ($10^{-35.2}$) and the K_{sp} of ZnSe ($10^{-25.4}$) drove the ion exchange between Zn^{2+} and Cd^{2+}. Additionally, trace amounts of Se ions were also detected in the solution and its concentration progressively increased when the $Cd(NO_3)_2$ concentration became higher, demonstrating that V_{Se} was generated in V_{Se}-ZCS during the ion exchange process.

The TEM images (Fig. S2) indicated that the doping of V_{Mo} into BMO did not destroy its Aurivillius-phase layered structure. The lattice spacings of 0.273 nm and 0.261 nm correspond to the (0 0 2) and (2 2 0) crystal planes of bismuth molybdate, respectively [29]. Fig. 1(f) presented an atomic-level HRTEM image of V_{Mo}-BMO with a local enlarged image. The atom intensity profiles of the two rectangular boxes in the enlarged image (Fig. 1(f)) were visualized in Fig. 1(g). The absence of Mo peak confirmed the existence of V_{Mo}. As illustrated in Fig. 1(h), the lattice spacing of 0.327 nm aligned with the (1 1 1) plane of ZnSe while the lattice spacing of 0.351 nm at the edge of ZnSe attributed to the (1 1 1) plane of CdSe, indicating that CdSe was produced on the outer surface of ZnSe nanoparticles after the ion exchange. Additionally, both the lattice distortion and V_{Se} (Fig. 1(i)) were observed on the outer surface of the ZnSe nanoparticle [30].

Fig. S3 and Fig. 2(a) displayed the SEM and HRTEM images of V_{Mo+Se}-BZCS, respectively. It was shown that numerous V_{Se}-ZCS nanoparticles were stacked on surfaces of V_{Mo}-BMO nanosheets. As shown in Fig. 2(b), the lattice spacings were ascribed to V_{Mo}-BMO (d = 0.273 nm, 0.261 nm), ZnSe (d = 0.327 nm), and CdSe (d = 0.351 nm), respectively. The distinct lattice distortion was observed at the interface between V_{Mo}-BMO and V_{Se}-ZCS, manifesting the creation of the V_{Mo}-BMO/V_{Se}-ZCS heterojunction interface [31]. All the elements of Bi, Mo, O, Zn, Se, and Cd (Fig. 2(c)) were uniformly distributed on the surface of V_{Mo+Se}-BZCS.

XPS analysis was performed to investigate the effects of V_{Mo} and V_{Se} doping on photocatalytic behavior of V_{Mo+Se}-BZCS. All the orbitals of Bi 4f, O 1s, Mo 3d, Se 3d, Zn 2p, and Cd 3d (Fig. S4(a)) were detected. The binding energy of Mo 3d, Bi 4f, and O 1s peaks of BMO/ZnSe (Fig. 2(d), Fig. S4(b), Fig. 2(e)) moved toward lower values in comparison with BMO while the binding energy of Se 3d and Zn 2p of BMO/ZnSe changed to higher values in comparison with ZnSe, implying the building of IEF at the BMO/ZnSe interface. Additionally, compared with BMO/ZnSe, both the peaks of Mo^{6+} $3d_{3/2}$ (235.66 eV) and Mo^{6+} $3d_{5/2}$ (232.52 eV) of V_{Mo+Se}-BZCS continued to shift toward lower binding energy [29] and both the deconvoluted peaks of Mo^{5+} $3d_{3/2}$ (234.28 eV) and Mo^{5+} $3d_{5/2}$ (229.12 eV) were observed for V_{Mo+Se}-BZCS. Thus, both the electron delocalization around Mo atom and the existence of V_{Mo} were testified [32]. Both the peaks of Bi^{3+} $4f_{5/2}$ and Bi^{3+} $4f_{7/2}$ (Fig. S4(b)) shifted toward lower binding energies [33]. Compared to BMO/ZnSe, the shift of the peaks ascribed to lattice oxygen (O_{latt}) and adsorbed oxygen (O_{ads}) of V_{Mo+Se}-BZCS (Fig. 2(e)) shifted to lower binding energies, implying the valence decrease of Mo adjacent to O atoms [34]. Additionally, the Zn 2p peak of V_{Mo+Se}-BZCS (Fig. 2(f)) shifted toward higher binding energy, suggesting that the doped V_{Se} functioned as trapped-electron centers. However, the Se 3d peak of V_{Mo+Se}-BZCS (Fig. S4(c)) shifted toward the lower binding energy in comparison with BMO/ZnSe, which was speculated to be due to the disturbance of the IEF in the heterojunction to the Se 3d binding energy. Fig. 1(i) showed that V_{Se} was more likely generated in ZnSe than in CdSe of V_{Mo+Se}-BZCS, suggesting the rationality of

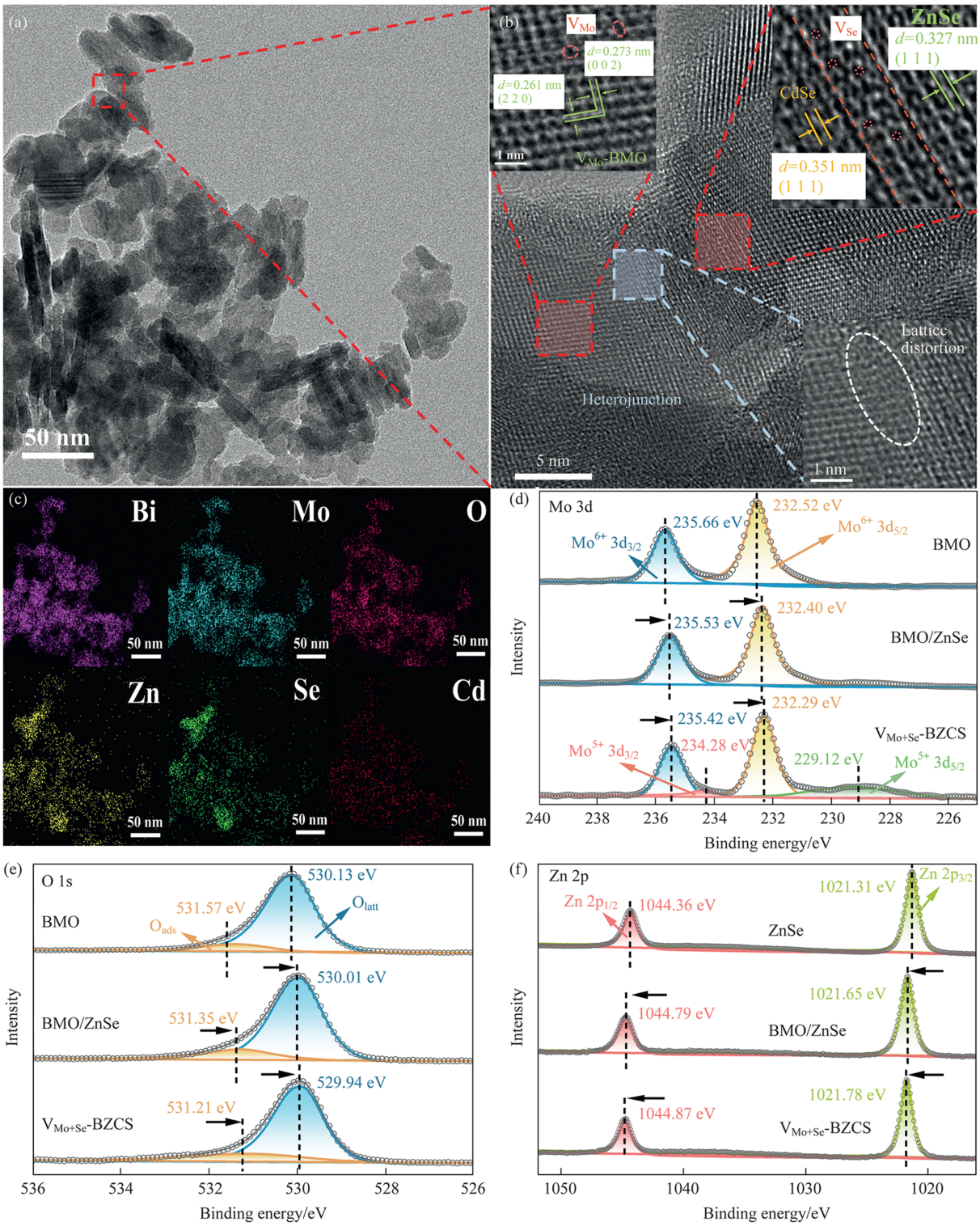


Fig. 2. (a) TEM images and (b) HRTEM images of V_{Mo+Se}-BZCS, (c-h) Energy dispersive spectroscopy mapping of V_{Mo+Se}-BZCS. High resolution XPS spectrum of (i) Mo 3d, (j) O 1s and (f) Zn 2p.

identifying the presence of V_{Se} by the changes of Zn 2p binding energy in the following in-situ XPS analysis.

3.2. Photochemical properties of the catalyst

The light absorption properties of the catalysts were evaluated by the UV-Vis DRS characterization (Fig. S5). The absorption edge of V_{Mo+Se}-BZCS was located at around 680 nm. Compared with the other catalysts, V_{Mo+Se}-BZCS exhibited the superior light response intensities in the range of 300–800 nm, indicating both the doping of V_{Mo} and V_{Se} enhanced the optical adsorption [35]. The calculated energy bandgaps (E_g) of BMO, V_{Mo}-BMO, ZnSe, and CdSe (Fig. S6) were determined to be 2.58 eV, 2.33 eV, 2.01 eV, and 1.72 eV, respectively, from the Tauc plots. The flat-band potentials

(E_{FB}) of V_{Mo}-BMO, ZnSe, and CdSe (Fig. S7) was estimated to be −0.25 V, −1.02 V, and −0.63 V *vs* SCE, respectively, from the Mott-Schottky plot. Furthermore, these values of E_{FB} were converted to the conduction band edge potential (E_{CB}) according to Eqs. (8) and (9). The E_{CB} of V_{Mo}-BMO, ZnSe, and CdSe were calculated to be −0.21 V, −0.98 V, and −0.59 V *vs* SHE, respectively. Subsequently, according to Eq. (12), the valence band edge potential (E_{VB}) of V_{Mo}-BMO, ZnSe, and CdSe were determined to be 2.12 V, 1.13 V, and 1.03 V *vs* SHE, respectively [36]. The electronic band structures of V_{Mo}-BMO, ZnSe, and CdSe were depicted in Fig. S8.

The *in-situ* XPS analysis was carried out to reveal the charge transfer mechanism of V_{Mo+Se}-BZCS. All the peaks of Mo 3d (Fig. 3(a)), Cd $3d_{3/2}$, Cd $3d_{5/2}$ (Fig. 3(c)), Bi 4f, and O 1s (Fig. S9) shifted toward the higher binding energy under LED irradiation, indicating the loss of the photogenerated electrons in both V_{Mo}-BMO and CdSe [27]. In contrast, both the Zn $2p_{1/2}$ and Zn $2p_{3/2}$ peaks (Fig. 3(b)) shifted toward the lower binding energy, demonstrating that V_{Se}-ZnSe gained the electrons. Fig. 3(d)–(f) exhibited the simulated work function (W_f) of V_{Mo}-BMO, ZnSe, and CdSe, respectively. Then, two charge transfer pathways in V_{Mo+Se}-BZCS were deduced (Fig. 3(g)). When V_{Mo}-BMO, CdSe, and V_{Se}-ZnSe are in close contact, the electrons spontaneously transfer from the surface of V_{Se}-ZnSe (with the highest fermi level (E_f)) to CdSe and then to V_{Mo}-BMO (with the lowest fermi level (E_f)) until the interfacial E_f reaches equilibrium [37]. Additionally, some electrons also directly transfer from V_{Se}-ZnSe to V_{Mo}-BMO at the V_{Se}-ZnSe/V_{Mo}-BMO interface. The two charge redistributions give rise to an internal electric field (IEF) oriented away from V_{Se}-ZnSe to CdSe and then to V_{Mo}-BMO and directly from V_{Se}-ZnSe to V_{Mo}-BMO, respectively, in the V_{Mo+Se}-BZCS heterojunction. The electron accumulations in V_{Mo}-BMO cause the band bending downward while the electron depletions in V_{Se}-ZnSe lead to the band bending upward. At the V_{Mo}-BMO/CdSe interface, the bands in V_{Mo}-BMO and CdSe bend downward and upward, respectively. Under LED light excitation, the electrons from the VB of V_{Mo}-BMO finally transfer to the CB of V_{Se}-ZnSe along two independent pathways under the combined action of IEF, interface band bending, and Coulomb forces. The electron transferring enables the photoelectrons and holes to accumulate in the CB of V_{Se}-ZnSe

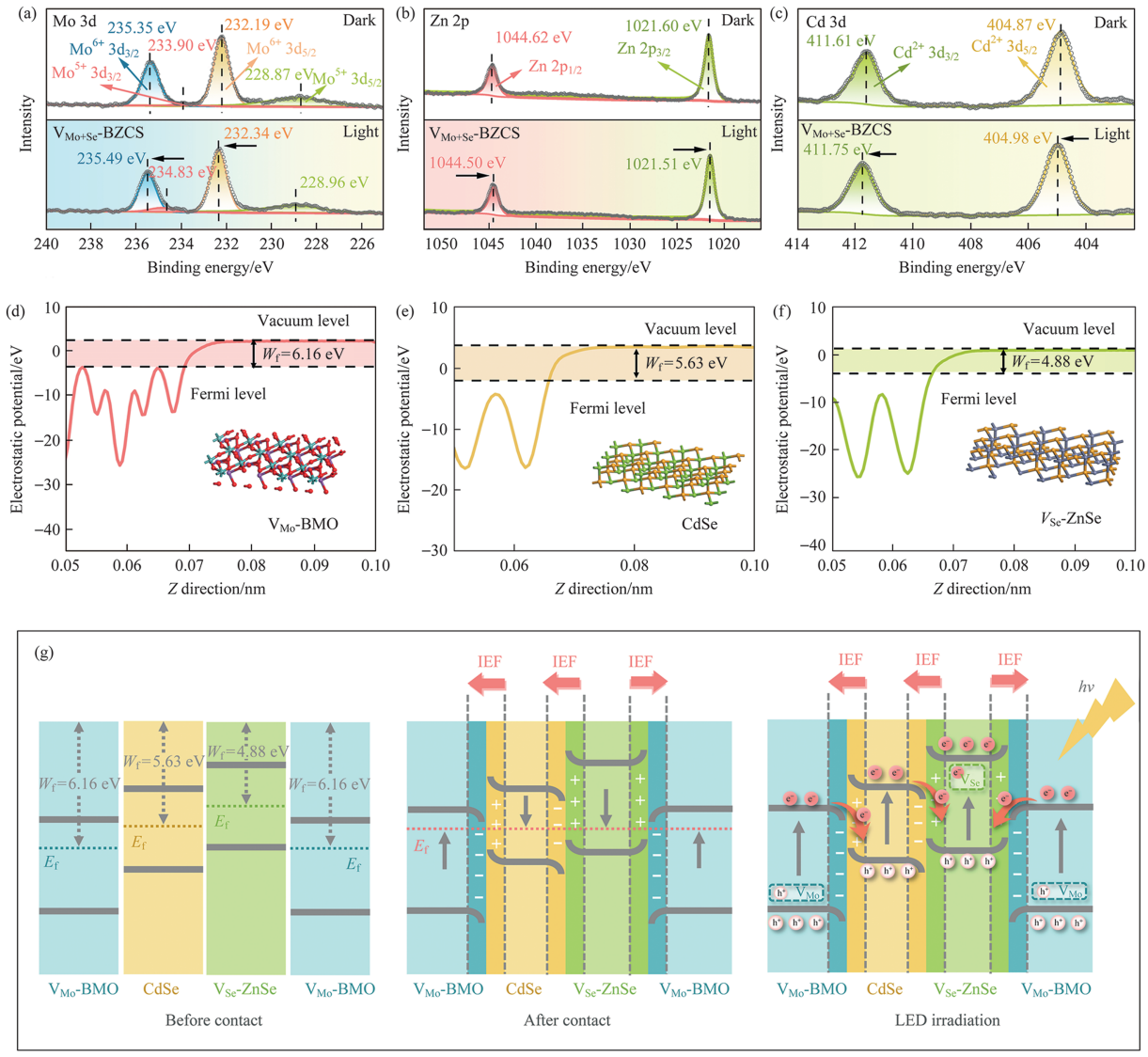


Fig. 3. *In situ* XPS high-resolution spectra of (a) Mo 3d, (b) Zn 2p, and (c) Cd 3d of V_{Mo+Se}-BZCS, simulated electrostatic potentials of (d) V_{Mo}-BMO, (e) V_{Se}-ZnSe, and (f) CdSe, (g) scheme of the charge transfer pathway and IEF of the dual S-scheme heterojunction in V_{Mo+Se}-BZCS.

and the VB of V_{Mo}-BMO respectively, thereby creating the dual S-scheme heterojunction [38]. Additionally, V_{Se} is able to confine the photoelectrons and increase the electron density around the V_{Se} sites in V_{Se}-ZnSe while V_{Mo} sites can effectively locate the holes in V_{Mo}-BMO, which not only suppresses the carrier recombination in the dual S-scheme heterojunction but also enhances the redox capability of V_{Mo+Se}-BZCS.

As observed in Fig. 4(a) and (b), the CB of V_{Mo}-BMO primarily derived from Bi p orbitals and Mo d orbitals, while the VB was chiefly composed of Bi p orbitals, Bi s orbitals, and O p orbitals. Fig. S10 manifested the comparison of the projected density of states (PDOS) between BMO and V_{Mo}-BMO and revealed that the defect states formed near the VB edge of V_{Mo}-BMO were composed of Bi s orbitals and O p orbitals. The defect states favorably narrowed the bandgap and facilitated electron transfer [39]. Furthermore, the differential charge density distribution maps demonstrated a distinct increase of the electron density around O atoms adjacent to V_{Mo} in V_{Mo}-BMO (Fig. S11), where red represents

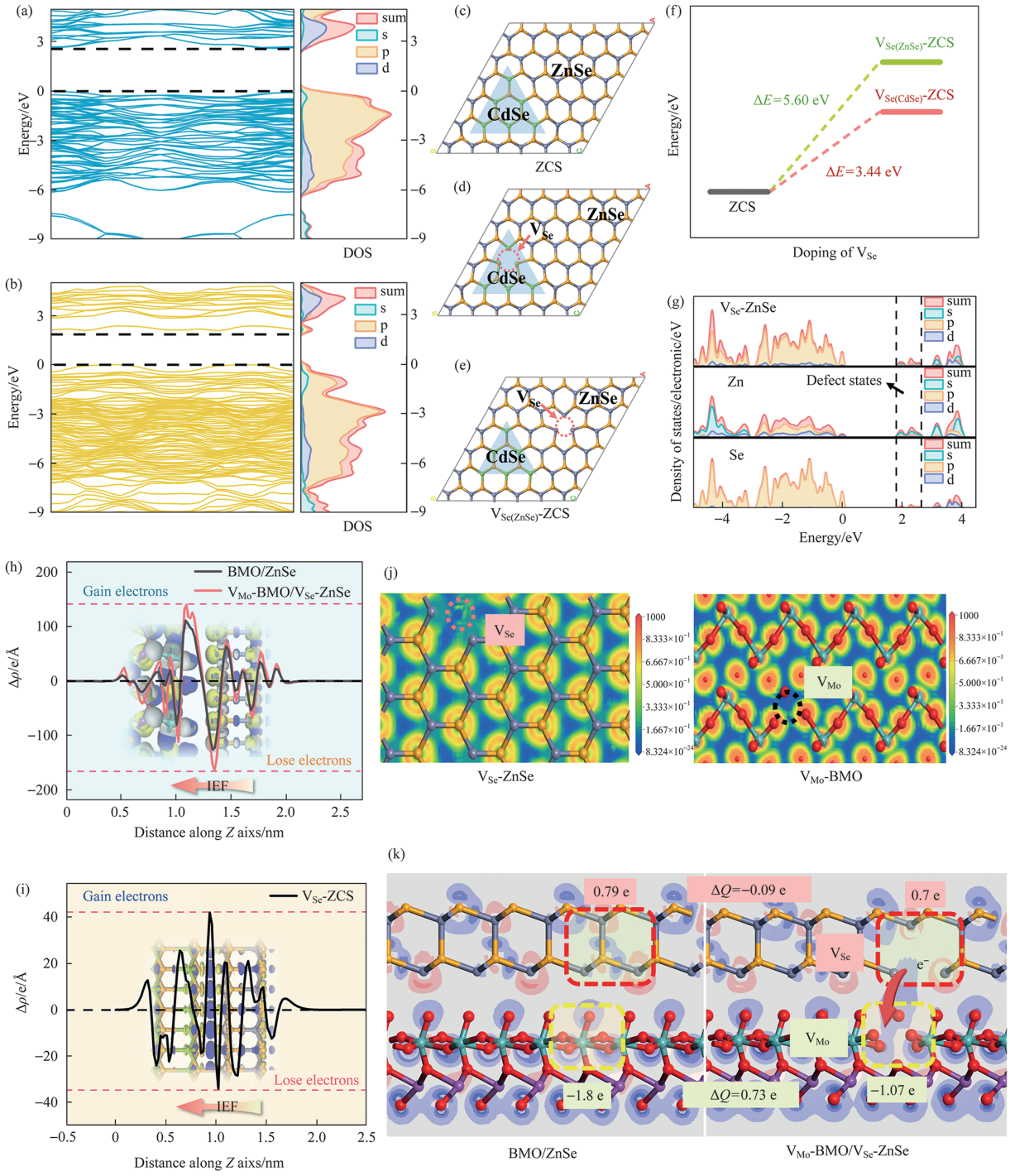


Fig. 4. Band structures and the related DOS of (a) BMO and (b) V_{Mo}-BMO, Models of (c) ZCS, (d) V_{Se}-ZCS with V_{Se} from CdSe, and (e) V_{Se}-ZCS with V_{Se} from ZnSe, (f) comparison of ΔE between $V_{Se(CdSe)}$-ZCS and $V_{Se(ZnSe)}$-ZCS, (g) PDOS of Zn and Se in V_{Se}-ZnSe, electron location function and planar-averaged differential charge density of (h) V_{Mo}-BMO/V_{Se}-ZnSe and (i) V_{Se}-ZCS, (j) electron localization function of V_{Se}-ZnSe and V_{Mo}-BMO, (k) differential charge distribution of BMO/ZnSe and V_{Mo}-BMO/V_{Se}-ZnSe.

electron depletion while blue indicates electron accumulation. The negatively charged center formed by V_{Mo} could trap the photogenerated holes in V_{Mo}-BMO, thereby suppressing electron-hole recombination and enhancing its oxidative degradation capability. A ZCS model was constructed and shown in Fig. 4(c). Zn atom was substituted with Cd atom along the [1 1 1] direction while the (1 1 1) plane was truncated for structural optimization. The optimized models of V_{Se}-ZCS with the V_{Se} from CdSe and ZnSe were illustrated in Fig. 4(d) and (e), respectively. The energy difference (ΔE) between the sum of the energy of the unit cell before and after V_{Se} doping was defined as the V_{Se} formation energy (Fig. 4(f)). The ΔE of $V_{Se(CdSe)}$-ZCS (3.44 eV) was much lower than $V_{Se(ZnSe)}$-ZCS (5.60 eV), indicating that V_{Se} was more prone to be formed in ZnSe than in CdSe. Fig. S12 displayed the optimized structural model of ZCS. It was observed that the structure of CdSe was stable and regular while the adjacent ZnSe configurations exhibited the obvious distortion, which coincided with the existence of V_{Se} and the lattice distortion displayed in Fig. 1(i). The differential charge distribution map of V_{Se}-ZCS (Fig. S13) indicated the electron accumulation around the V_{Se} site. The projected density of states (PDOS) spectra for V_{Se}-ZnSe and ZnSe were shown in Fig. 4(g) and Fig. S14, respectively. The doping of V_{Se} in ZnSe directly produced the defect states in its bandgap, which derived dominantly from Zn s orbitals.

Fig. S15 manifested the V_{Mo}-BMO/V_{Se}-ZnSe heterojunction model and the V_{Se}-ZCS model while their planar averaged charge densities were plotted in Fig. 4(h) and (i), respectively, to visualize the transfer of electrons at the heterojunction interface. The negative and positive values of $\Delta\rho$ in its distribution along the *z*-direction (vertical to the interface) denoted the charge depletion and accumulation, respectively. An IEF directed from V_{Se}-ZnSe to V_{Mo}-BMO was constructed owing to the electron gains in V_{Mo}-BMO and the electron losses in V_{Se}-ZnSe. As demonstrated in Fig. 4(h), the charge density at the V_{Mo}-BMO/V_{Se}-ZnSe interface (red line) changed higher than the BMO/ZnSe interface (black line), indicating that the dopings of V_{Se} and V_{Mo} enhanced the IEF strength [40]. Fig. 4(i) verified the IEF direction in V_{Se}-ZCS from V_{Se}-ZnSe to CdSe as well. Fig. 4(j) displayed that both the electron localization function (ELF) values around the V_{Se} site in V_{Se}-ZnSe and around the V_{Mo} site in V_{Mo}-BMO were significantly lower than that around the other Se and Mo sites Consequently, the highly delocalized electron distribution around both the V_{Se} and V_{Mo} site facilitated the transferring of more electrons [41]. As observed in Fig. 4(k), the differential charge distribution in the region between V_{Mo} and V_{Se} site manifested a spontaneous charge transfer pathway at the V_{Mo}-BMO/V_{Se}-ZnSe interface. The Muliken charge changes (ΔQ) between before and after the doping of V_{Mo} and V_{Se} were quantified as well. The positive ΔQ of V_{Mo} site and the negative ΔQ of V_{Se} site demonstrated the electron transfer from V_{Mo} to V_{Se} [29]. Actually, the electrons transferred evidently from the Zn atoms adjacent to V_{Se} sites to the O atoms adjacent to V_{Mo} site through V_{Mo}-BMO/V_{Se}-ZnSe interface (Fig. 4(k)) because the electronegativity of O (3.44) was much higher than Zn (1.65). The electron transfer direction was the same as the IEF direction, enhancing the IEF strength accordingly. During the photodegradation, the doping of V_{Mo} and V_{Se} encouraged the formation of new photoinduced hole acceptors and new photoinduced electron acceptors in V_{Mo}-BMO and V_{Se}-ZnSe, respectively, which was expected to promote the electron-hole recombination along with the IEF.

3.3. Efficient photoinduced electron-hole separation in the catalyst

Transient photocurrent response (TPR) analysis (Fig. 5(a)) were performed to detect the photoinduced electron-hole separation in the presence of different catalysts. V_{Mo+Se}-BZCS owned the highest photocurrent intensity among all the catalysts, further confirming that the engineered dual vacancies promoted the photoelectron-hole separation efficiency of the dual S-scheme heterojunction. The Nyquist diagrams of different catalysts (Fig. 5(b)) displayed that V_{Mo+Se}-BZCS had the shortest curvature radius, suggesting the existence of a rapid charge transfer pathway [42,43]. The cyclic voltammetry (CV) profiles of the electrodes modified using different catalysts (Fig. 5(c)) in Na_2SO_4 electrolyte under LED irradiation exhibited that V_{Mo}-BZCS owned the augmented oxidation peak at 0.024 V *vs.* SCE while V_{Se}-BZCS possessed the intensified reduction peak at −0.794 V *vs.* SCE in comparison with BZCS, signifying that the doping of V_{Mo} and V_{Se} improved the oxidative and the reductive activity, respectively [44]. V_{Mo+Se}-BZCS further showed the strongest reduction and oxidation peaks at 0.105 V *vs*. SCE and −0.863 V *vs.* SCE, respectively, demonstrating that V_{Mo} and V_{Se} jointly enhanced the redox activity.

Both the fs-TAS measurements of BZCS and V_{Mo+Se}-BZCS were carried out to uncover the electron transfer mechanism in photocatalysis. As shown in Fig. 5(d) and (g), the fs-TAS spectra of BZCS possessed an excited-state absorption (ESA) peak at around 510 nm and a broad ground-state bleach (GSB) peak at 640-700 nm. Nevertheless, two distinct GSB peaks could be distinguished from the fs-TAS spectra of V_{Mo+Se}-BZCS. Fig. 5(e) and (h) presented the 2D pseudo-color maps of fs-TA spectra for BZCS and V_{Mo+Se}-BZCS, respectively. BZCS demonstrated an individual ESA band and an individual GSB band, respectively, whereas V_{Mo+Se}-BZCS exhibited two prominent GSB bands. The GSB signals generally originate from electron transitions from VB to CB in the photocatalyst and serve as indicators for photoelectron yield or charge transfer capability [12]. As observed in Fig. 5(h), the first GSB band in the delay time range of 1-10 ps was attributed to the photoinduced electron transfer and combination between V_{Mo} site and V_{Se} site near the V_{Mo}-BMO/V_{Se}-ZnSe interface while the second GSB band in the delay time range of 100-1000 ps was accredited to the charge recombination for the trapped holes and electrons by V_{Mo} site and V_{Se} site, respectively. They denoted two independent photoinduced charge transfer pathways once under the photoexcitation. The distinct ESA signals between the two GSB bands suggested the electron transfer from the CB of V_{Mo}-BMO to the VB of V_{Se}-ZnSe. Together with Fig. 3(g), the two photoinduced charge transfer pathways were presumed to correspond to V_{Mo}-BMO(VB) → CdSe → V_{Se}-ZnSe(CB) through the V_{Mo}-BMO/CdSe/V_{Se}-ZnSe interface (Fig. 5(j)) and V_{Mo} → V_{Se} through the V_{Mo}-BMO/V_{Se}-ZnSe interface (Fig. 5(k)). The short delay time of V_{Mo} → V_{Se} denoted the formation of a new fast photogenerated charge transferring pathway, which worked together with the other pathway to boost the production of more holes on the VB of V_{Mo}-BMO and more electrons on the CB of V_{Se}-ZnSe. Accordingly, the redox capability of the catalyst was greatly enhanced [45].

Fig. 5(f) and (i) manifested the fitting results of GSB recovery kinetics for BZCS and V_{Mo+Se}-BZCS, respectively. Three lifetime components were determined for both BZCS and V_{Mo+Se}-BZCS, implying three major electron quenching pathways. The scheme of the photogenerated carrier decay pathways in BZCS and V_{Mo+Se}-BZCS was presented in Fig. 5(j) and (k), respectively. The lifetime of dozens of picoseconds timescale (τ_1) denotes the short-lived charge recombination process caused by the trap state (TS) in V_{Mo}-BMO [46]. The τ_1 for V_{Mo+Se}-BZCS was lower than that for BZCS. Actually, V_{Mo} and V_{Se} could trap the photogenerated holes and electrons, respectively, to decrease both the amounts of the holes and electrons transferred to the trap state, which suppressed the trap state-assisted carrier recombination. Another lifetime of hundreds of picoseconds timescale (τ_2) denotes the recombination of electrons from CB and holes from VB [47]. Compared to BZCS, the

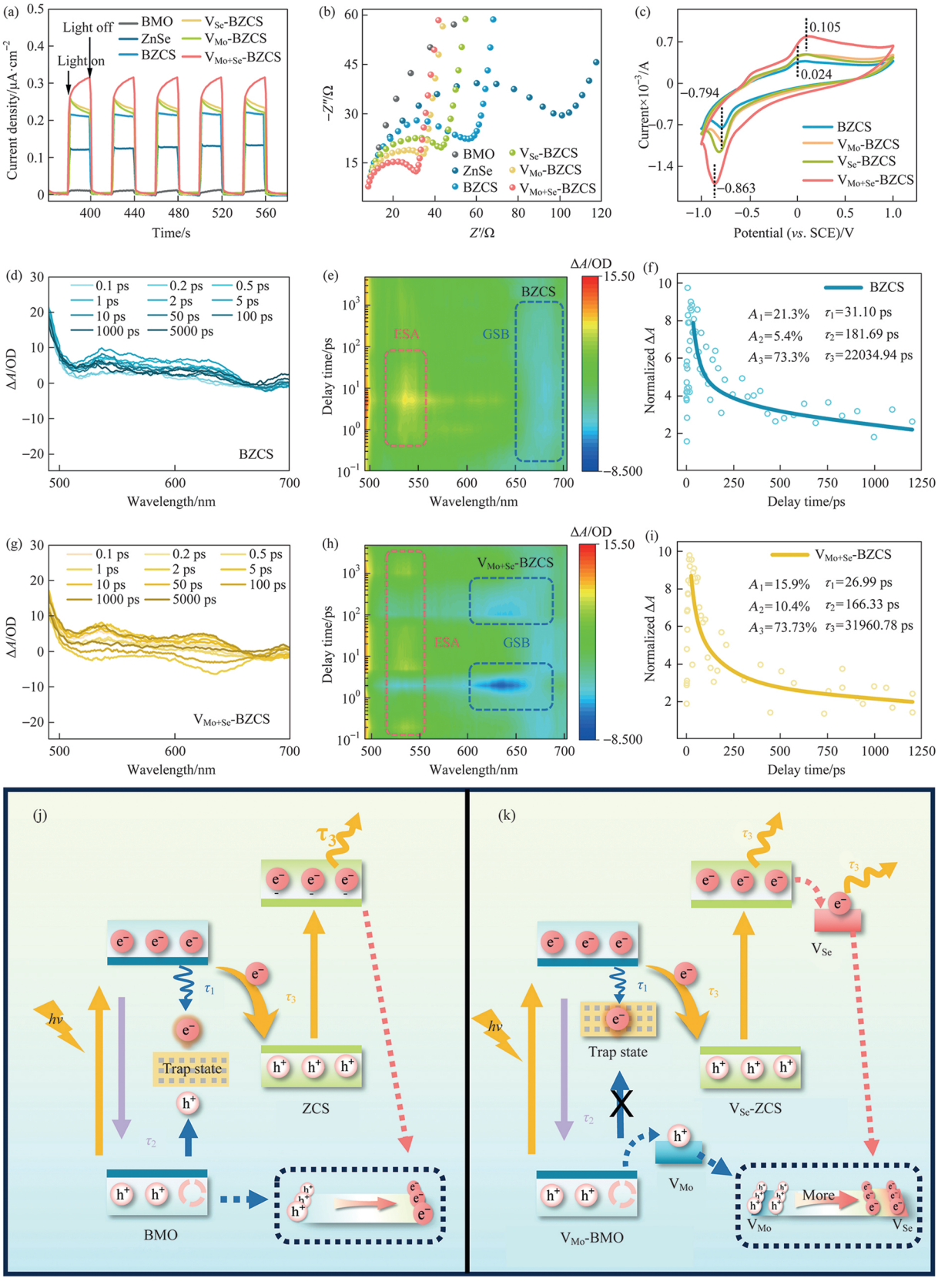


Fig. 5. (a) Transient photocurrent response, (b) Nyquist diagram, and (c) Cyclic voltammetry (CV) curve of different catalysts, selected transient absorption spectra at specific time scales of (d) BZCS and (g) V_{Mo+Se}-BZCS, 2D pseudo-colored fs-TAS spectra of (e) BZCS and (h) V_{Mo+Se}- BZCS, Normalized GSB recovery kinetics fitting curves of (f) BZCS and (i) V_{Mo+Se}-BZCS probed at 631 nm, photoinduced electron decay pathways for (j) BZCS and (k) V_{Mo+Se}-BZCS.

shorter τ_2 of V_{Mo+Se}-BZCS was due to the recombination of the electrons from the V_{Se} in V_{Se}-ZCS and the holes from the V_{Mo} in V_{Mo}-BMO. The V_{Se}-V_{Mo} recombination evidently decreased the amounts of the photoelectrons involved in CB-VB recombination [48], thereby improving the redox capability of V_{Mo+Se}-BZCS. The longest lifetime of nanosecond timescale (τ_3) was attributed to the photoelectron transfer through heterojunctions toward the V_{Se}-ZCS surface [49]. Conversely, the value of τ_3 for V_{Mo+Se}-BZCS larger than that for BZCS demonstrated the higher carrier transferring rate through the heterojunction interface toward the surface of V_{Se}-ZCS, which led to the electron enrichment on the surface of V_{Se}-ZCS for redox reactions [50]. Therefore, V_{Mo} and V_{Se} not only suppressed the photogenerated electron-hole recombination in the heterojunction but also provided abundant free-migrating electrons and holes on the catalyst's surface, ultimately endowing V_{Mo+Se}-BZCS with superior photocatalytic activity.

3.4. Photocatalytic degradation experiment for TC and Cr(VI)

The photocatalytic performance of different photocatalysts were evaluated for simultaneous TC degradation and Cr(VI) reduction. As seen in Fig. 6(a)–(f), almost all the catalysts reached the adsorption equilibrium during the initial 30 min dark adsorption period. V_{Mo+Se}-BZCS achieved both the highest TC degradation efficiency of 90.1% (Fig. 6(a)) and the highest Cr(VI) reduction efficiency of 95.2% (Fig. 6(d)) at 120 min among the catalysts while BZCS owned the TC degradation efficiency of 75.1% and the Cr(VI) reduction efficiency of 74.0%. The effects of V_{Mo} and V_{Se} concentration on the catalytic performance of V_{Mo+Se}-BZCS was investigated. V_{Mo} concentration was adjusted by changing the immersion time of BMO in the deep eutectic solvent (DES) while V_{Se} concentration was tuned by controlling the Cd^{2+} concentration in the ion exchange process between Cd^{2+} and Zn^{2+}. Additionally, as displayed in Fig. 6(a)–(f), both the TC degradation efficiency and the Cr(VI) reduction efficiency of V_{Mo+Se}-BZCS were obviously higher than V_{Mo}-BZCS or V_{Se}-BZCS alone because the doping of V_{Mo} and V_{Se} magnified the BPEs between TC and Cr(VI). In the degradation, TC and Cr(VI) consumed the photoinduced holes on the VB of V_{Mo}-BMO and the photoinduced electrons from the CB of V_{Se}-ZCS, respectively, serving as sacrificial agents for one another, thereby inhibiting the photogenerated electron-hole recombination. Likewise, the doping of V_{Mo} and V_{Se} performed as the photoinduced holes trapped centers in V_{Mo}-BMO and the photoinduced electrons trapped centers in V_{Se}-ZCS, respectively, which restricted the electron-hole recombination during the degradation as well. Therefore, the dual-vacancy engineering strategy greatly amplified

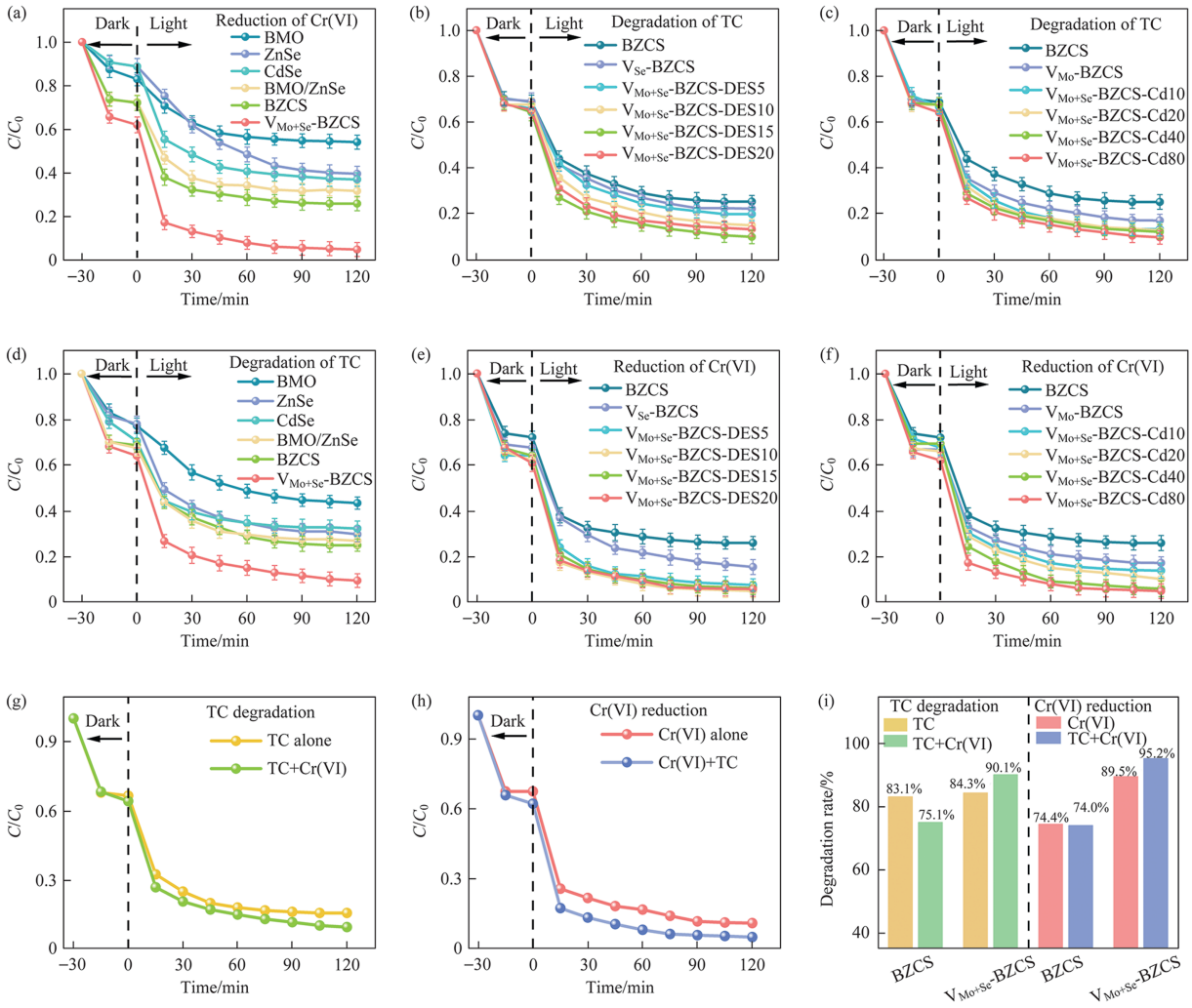


Fig. 6. Photocatalytic TC degradation curves and Cr(VI) reduction curves of (a, d) different catalysts, (b, e) the catalysts with different DES degradation times, and (c, f) the catalysts with different $Cd(NO_3)_2$ concentrations, (g) TC degradation curves and (h) Cr(VI) reduction curves of V_{Mo+Se}-BZCS in the wastewater containing both TC and Cr(VI), TC alone, and Cr(VI) alone, (i) comparison of TC degradation curves and Cr(VI) reduction efficiency of BZCS and V_{Mo+Se}-BZCS.

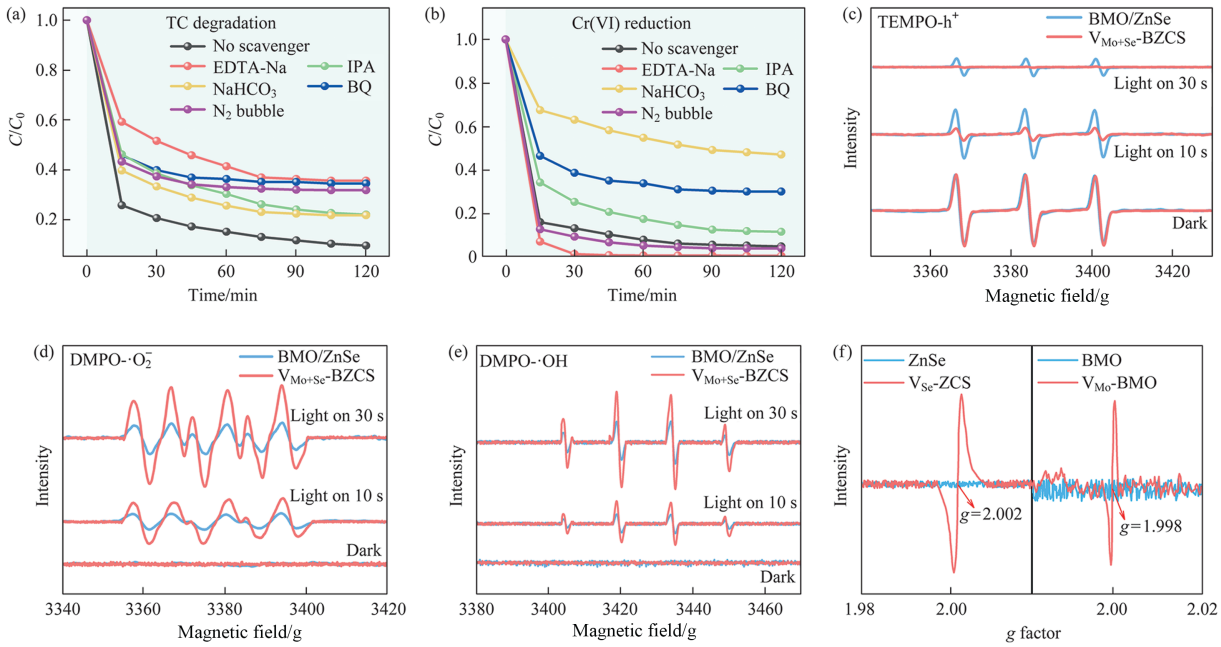


Fig. 7. (a) TC degradation curves and (b) Cr(VI) reduction curves for different quenchers in the presence of V_{Mo+Se}-BZCS, ESR spectra of (c) h+, (d)·O−2, (e) ·OH generated under dark and illumination conditions in the presence of V_{Mo+Se}-BZCS, and (f) ESR spectra of V_{Se} and V_{Mo}.

the BPEs, and hence increased both the TC and Cr(VI) degradation efficiency.

The TC and Cr(VI) degradation efficiency for the wastewater containing TC alone, Cr(VI) alone, and both TC and Cr(VI) were compared for BZCS and V_{Mo+Se}-BZCS, respectively. For BZCS, the TC degradation efficiency for the wastewater containing TC alone was higher than that for the wastewater containing both TC and Cr(VI) (Fig. S16), denoting that Cr(VI) owned an inhibitory effect on TC degradation. It was because that Cr(VI) reduction competed for the consumption of photogenerated electrons from the CB of ZnSe that would otherwise be used to generate the ROS effective for TC degradation, such as ·O−2 and ·OH. Additionally, although the Cr(VI) reduction efficiency for the wastewater containing both TC and Cr(VI) was higher than that for the wastewater containing both Cr(VI) alone during the first 60 min of the reduction, both of the Cr(VI) reduction efficiency were basically equal when the Cr(VI) reduction approached 120 min, suggesting that the TC and Cr(VI) degradation catalyzed by BZCS showed no BPEs. In contrast, for V_{Mo+Se}-BZCS, both the TC and Cr(VI) degradation efficiency for the degradation of the wastewater containing both TC and Cr(VI) exceeded those for the degradation of the wastewater containing TC or Cr(VI) alone (Fig. 6(g) and (h)). It was also demonstrated that the doped V_{Mo} and V_{Se} amplified the BPEs between TC and Cr(VI) and the resultant photoinduced hole and electron centers improved the catalyst's redox performance.

Particularly, increasing the immersion time led to the highest TC degradation efficiency of for V_{Mo+Se}-BZCS-DES15 (Fig. 6(b)) whereas exerted limited effects on Cr(VI) reduction efficiency (Fig. 6(e)). Excessive immersion time of BMO into DES generated overabundant V_{Mo}, which even wrongly acted as the electron-hole recombination centers, and reduced the TC degradation efficiency [40]. Additionally, an increased Cd^{2+} concentration resulted into a progressively higher Cr(VI) reduction efficiency (Fig. 6(c)), which reached a maximum of 98.2% when the Cd^{2+} concentration was 80 mmol·L^{-1}, whereas Cd^{2+} concentration only marginally promoted the TC degradation efficiency (Fig. 6(f)). V_{Mo} only promoted the TC degradation because it trapped the photoinduced holes which could directly oxidize TC and break the large TC molecule into small molecules. Similarly, V_{Se} facilitated the Cr(VI) reduction because it trapped the photoinduced electrons.

Fig. S17(a) and S17(d) displayed that both the TC degradation efficiency and Cr(VI) reduction efficiency initially increased and subsequently decreased with the gradually increased mass fraction of V_{Se}-ZCS in V_{Mo+Se}-BZCS. The TC degradation efficiency and the Cr(VI) reduction efficiency were the highest at 90.1% and 95.2%, respectively, with the V_{Se}-ZCS mass fraction of 25% [51]. Fig. S17(b) and S17(e) demonstrated that both the TC degradation efficiency and the Cr(VI) reduction efficiency progressively rose with the increased V_{Mo+Se}-BZCS loading in the degradation. Fig. S17(c) and S17(f) highlighted the effects of pH on the simultaneous degradation of TC and Cr(VI). The TC degradation efficiency was the highest at under neutral conditions while the Cr(VI) reduction efficiency steadily declined with the pH value changing from 2 to 12. Cr(VI) exist in the form of $Cr_2O_7^{2-}$ and $HCrO_4^-$ under acid conditions, which favored the Cr(VI) reduction [52], while TC exist as TCH^{3+} when pH is greater than 3.3 and less than 7.7, which is resistant to be degraded [53].

Table S3 compared the photocatalytic performance of V_{Mo+Se}-BZCS and some other reported catalysts for the simultaneous removal of TC and Cr(VI). V_{Mo+Se}-BZCS possessed the superior catalytic performance under both LED and xenon lamp irradiation, respectively, among all the listed catalysts. The TC degradation efficiency and the Cr(VI) reduction efficiency of V_{Mo+Se}-BZCS was 98.9% and 99.5% under xenon lamp irradiation, respectively, by the end of the degradation. Actually, as seen in Fig. S18(a) and S18(b), these two efficiencies had achieved 96.1% and 96.4%, respectively, when the degradation proceeded for 60 min. The TC degradation efficiency and the Cr(VI) reduction efficiency of V_{Mo+Se}-BZCS under LED irradiation was 90.1% and 95.2%, respectively. The difference in the two efficiencies between under the xenon lamp and under LED irradiation was attributed to the factor that the xenon lamp owned a broader spectral range and higher light intensity than LED. However, LED was still competitive because its power (40 W) was only one-fifth of the of xenon Lamp (200 W) and its lifetime was

commonly 10 times longer than of the conventional xenon Lamp. In the five-cycle photodegradation tests, V_{Mo+Se}-BZCS exhibited a high cyclability. As exhibited in Fig. S18(c) and S18(d), the TC degradation efficiency and Cr(VI) reduction efficiency decreased by only 4.8% and 5.2%, respectively, after the five degradation cycles.

The major ROS responsible for TC degradation and Cr(VI) reduction were determined through the free radical quenching experiment and electron spin resonance (ESR) analysis. EDTA-Na, IPA, BQ, and $NaHCO_3$ was exploited as the quenchers for hole, ·OH, ·O−2, and photoinduced electron, respectively [54,55]. As shown in Fig. 7(a) and (b), the photoinduced holes exerted the most significant effect on TC degradation, followed by $\cdot O_2^-$ and ·OH, while the photoinduced electrons played the greatest role in Cr(VI) reduction because the Cr(VI) reduction efficiency sharply decreased after $NaHCO_3$ quenched the electrons in the heterojunction. It was noted that the added EDTA-Na quenched a lot of photoinduced holes in the catalyst and suppressed most of the electron-hole recombination. Consequently, substantial photoinduced electrons near the CB of V_{Mo+Se}-BZCS was able to efficiently reduce Cr(VI). Fig. 7(c)–(e) indicated that all the signals of h^+, $\cdot O_2^-$, and ·OH were successfully detected for both the photocatalytic degradation system in the presence of BMO/ZnSe and V_{Mo+Se}-BZCS. Remarkably, the peak intensity of h^+ possessed a negative correlation with its amount while both the peak intensity of ·O−2 and ·OH owned a positive correlation with its amount. All the amounts of the above three ROS generated in the presence of V_{Mo+Se}-BZCS were distinctly higher than those in the presence of BMO/ZnSe, highlighting the promoting effect of the fast photoinduced charge transferring pathway on the photocatalytic generation of ROS. It was because that the fast pathway led to the generation of more photoinduced h^+ and electrons, which directly drove the formation of ·OH and $\cdot O_2^-$ [56].

The electrostatic potential map, the lowest unoccupied molecular orbital (LUMO), the highest occupied molecular orbital (HOMO), and the Fukui functions (the electrophilicity (f^-), the nucleophilicity (f^+), and the radical attack susceptibility (f^0)) of TC were displayed in Fig. S19(a)–S19(d), respectively. HOMO was mainly localized near N atom (45) and the adjacent two methyl groups, manifesting that both the C (47-48) atoms and N (45) atom were more susceptible to be attacked by the electrophilic radicals

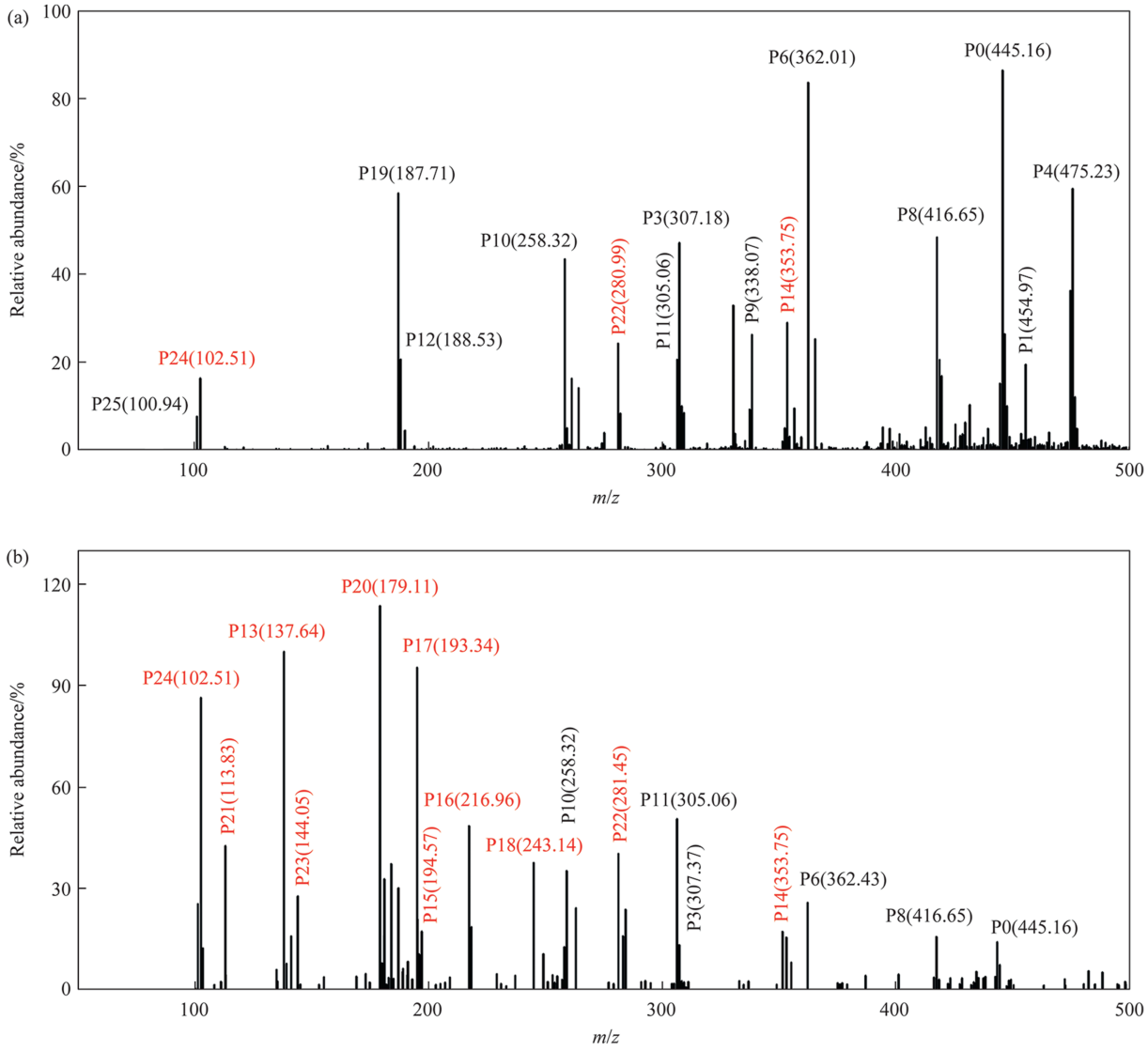


Fig. 8. HPLC-MS spectra of the degradation solutions (a) 15 min and (b) 90 min after the degradation started for the TC and Cr(VI) wastewater in the presence of V_{Mo+Se}-BZCS, (c) possible degradation pathways of TC in the presence of V_{Mo+Se}-BZCS.

(h^+ and ·OH). Additionally, LUMO was primarily placed near carbonyl group, benzene ring, and hydroxyl group, rendering them attacked by such nucleophilic radicals as $\cdot O_2^-$ h^+ and ·OH preferred to target the atoms of C (47-48) and N (45) with the high f^- value, removing both the hydroxyl and amine groups and opening the cycloalkane, while $\cdot O_2^-$ preferentially broke the nucleophilic sites with the high f^+ value and opened the aromatic ring at C (1-15).

3.5. Effects of vacancies on the degradation intermediate and pathways

HPLC-MS characterization was carried out for modifying the intermediate products 15 and 90 min after the start of the degradation in the presence of BMO/ZnSe and V_{Mo+Se}-BZCS, respectively. Fig. S20(a) and S20(b) exhibited the mass-to-charge ratio (m/z) values of the intermediate products during the degradation for BMO/ZnSe while Fig. 8(a) and (b) showed those for V_{Mo+Se}-BZCS. Four pathways of the TC degradation in the presence of V_{Mo+Se}-BZCS were hypothesized and were depicted in Fig. 8(c). Both the red product names (Fig. 8(b)) and the red structure formulas (Fig. 8(c)) represented the small molecule intermediates that were not generated during the degradation in the presence of BMO/ZnSe but were produced in the presence of V_{Mo+Se}-BZCS. It was shown that some complex polycyclic aromatic hydrocarbons, such as P2, P6, and P8, could still be detected even 90 min after the degradation in the presence of BMO/ZnSe. Nevertheless, more ROS produced in the presence of V_{Mo+Se}-BZCS were able to further break the above complex molecules to produce the small molecule intermediates, including P15, P17, P21, and P24.

The acute and chronic toxicity of all the degradation intermediates (P0-P25) were predicted using ECOSAR algorithm. The LC50 and EC50 of fish, daphnia and green algae were used as the indicative factor of acute toxicity while the CHV was utilized as the indicative factor of chronic toxicity (Fig. S21(a)). The lower the indicative factors were, the higher the toxicity was. The toxicity of the majority of the degradation intermediates detected in pathway 1, 2, 3, and 4 for the degradation in the presence of V_{Mo+Se}-BZCS were considerably lowered in comparison with TC. Particularly, the small molecule intermediates only detected during the degradation in the presence of V_{Mo+Se}-BZCS, such as P13, P15, P16, P17, P21, and P24, exhibited low toxicity or even non-toxic. The biotoxicity of the degradation solutions of the TC and Cr(VI) wastewater after the photocatalytic degradation of 180 min in the presence of different photocatalysts were assessed with *E. coli* O157:H7. As displayed in Fig. S21(b), the viable cell count of *E. coli* O157:H7 in the degradation solution for different catalysts

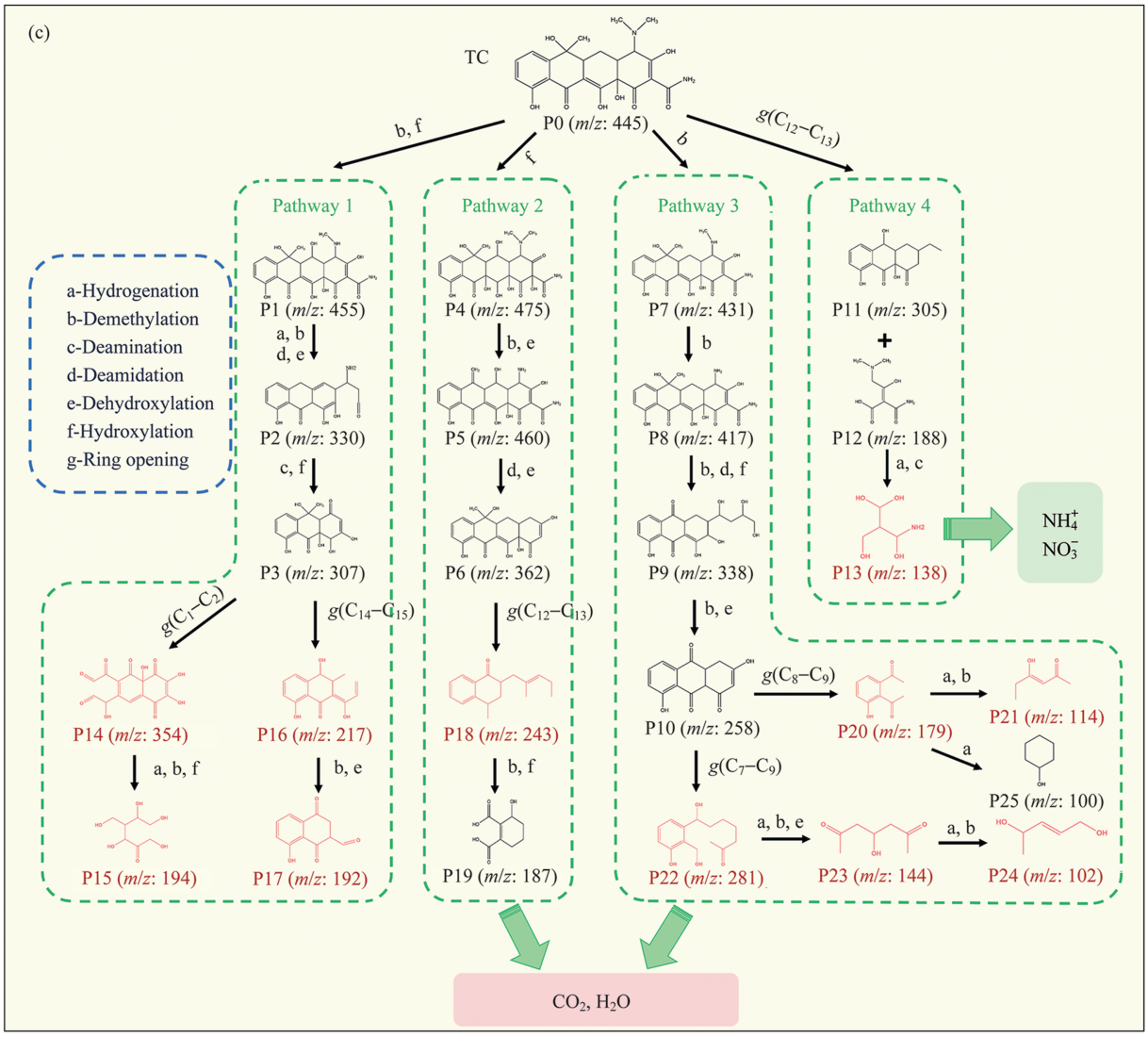


Fig. 8. (*continued*).

decreased in the sequence of V_{Mo+Se}-BZCS > V_{Se}-BZCS > V_{Mo}-BZCS > BZCS > BMO. The colony number ratio for V_{Mo+Se}-BZCS (Fig. S22) was the highest and even reached 100.3% after 12 h of incubation, manifesting that the degraded solutions after 180 min of the degradation of wastewater in the presence of V_{Mo+Se}-BZCS possessed the lowest biotoxicity. The ^{1}H NMR spectrum of the degraded solution (Fig. S21(c)) displayed no observable peaks of organic compounds, demonstrating complete degradation of TC into small-molecule inorganic compounds. As displayed in Fig. S23, the TOC removal for the TC degradation process catalyzed by BMO/ZnSe and $V_{Mo\ +\ Se}$-BZCS was calculated to be 34.2% and 60.2% after the 120 min of the photocatalytic degradation period.

The photocatalytic mechanism of V_{Mo+Se}-BZCS for simultaneous TC degradation and Cr(VI) reduction was proposed (Fig. S24). In the heterojunction, an IEF from ZnSe to BMO was built because the work functions were in the order of V_{Mo}-BMO > CdSe > V_{Se}-ZnSe in V_{Mo+Se}-BZCS. The introduction of V_{Mo} and V_{Se} into the oxidation ends and the reduction ends of the S-scheme heterojunction added a new electron transfer pathway directly from V_{Se}-ZnSe to V_{Mo}-BMO and generated an extra IEF. The directions of the resultant two IEFs were the same, thereby enhancing the IEF intensity and constructing a dual S-scheme heterojunction constructure of V_{Mo+Se}-BZCS. Once upon the light irradiation, V_{Mo} and V_{Se} could trap the photogenerated holes and electrons, respectively, which caused a rapid photoinduced charge transfer pathway ($V_{Mo} \rightarrow V_{Se}$) through the heterojunction interface under the Coulomb force in the IEF with the direction V_{Se}-ZnSe→V_{Mo}-BMO. Consequently, the hole-electron recombination was considerably prevent in both V_{Se}-ZnSe and V_{Mo}-BMO. The photogenerated electrons accumulated in the CB of V_{Se}-ZnSe reduced Cr(VI) into Cr(III) while the holes accumulated in the VB of V_{Mo}-BMO oxidized and degraded TC into small molecules. Additionally, the photogenerated electrons and holes were able to produce the ROS effective for TC degradation, including $\cdot O_2^-$ and ·OH. The whole photocatalytic degradation process includes the reactions shown as from Eq. (1) to Eq. (7).

$$\text{Photocatalytic} + h\nu \rightarrow e^- + h^+ \quad (1)$$

$$V_{Mo} + h^+ \rightarrow V_{Mo}\text{-}h^+ \quad (2)$$

$$V_{Se} + e^- \rightarrow V_{Se}\text{-}e^- \quad (3)$$

$$H_2O + V_{Mo}\text{-}h^+ \rightarrow \cdot OH + H^+ + V_{Mo} \quad (4)$$

$$O_2 + V_{Se}\text{-}e^- \rightarrow \cdot O{-}2 + V_{Se} \quad (5)$$

$$Cr(VI) + 3V_{Se}\text{-}e^- \rightarrow Cr(III) + 3V_{Se} \quad (6)$$

$$h^+/\cdot O{-}2/\ \cdot OH + TC \rightarrow H_2O + CO_2 \quad (7)$$

4. Conclusions

This study successfully constructed a dual-vacancy engineered dual S-scheme heterojunction (V_{Mo+Se}-BZCS) by DES impregnation and ion exchange methods. HRTEM images confirmed the targeted doping of V_{Mo} and V_{Se} into BMO and ZnSe, respectively, and the lattice distortion at the V_{Mo}-BMO/V_{Se}-ZCS interface was observed as well. The electronic band structures of V_{Mo}-BMO, ZnSe, and CdSe were depicted according to the UV-Vis DRS and Mott-Schottky characterization results, verifying the dual S-scheme heterojunction structure of V_{Mo+Se}-BZCS together with the XPS analysis. DFT simulation revealed that more electrons spontaneously transferred through the heterojunction interfaces from the neighboring Zn atoms near V_{Se} to the V_{Mo} site, which enhanced the IEF strength accordingly. Both *in-situ* XPS and fs-TAS analysis certified the formation of a fast charge transfer pathway through the V_{Mo}-BMO/V_{Se}-ZnSe interface upon LED irradiation. Additionally, V_{Mo} and V_{Se} acted as the photoexcited hole and electron trapping centers, respectively, thereby efficiently promoting the electron-hole separation of V_{Mo+Se}-BZCS. Consequently, V_{Mo+Se}-BZCS showed the TC degradation efficiency of 90.1% and the Cr(VI) reduction efficiency of 95.2% upon LED irradiation and the TC degradation efficiency of 98.9% and the Cr(VI) reduction efficiency of 99.5% upon xenon lamp irradiation, during the photocatalytic degradation of the wastewater containing both tetracycline (TC) and Cr(VI). All the values were competitive in comparison with some other reported catalysts. The dual doping of V_{Mo} and V_{Se} were confirmed to magnify the bi-directional promotion effects (BPEs) between TC and Cr(VI) in the presence of V_{Mo+Se}-BZCS.

CRediT Authorship Contribution Statement

Pengfei Tian: Writing – original draft, Visualization, Validation, Investigation, Formal analysis, Data curation. Yunan Shen: Writing – original draft, Visualization, Validation, Software, Formal analysis, Data curation. Yuzhe Hua: Visualization, Validation, Software, Conceptualization. Xiyu Zou: Writing – original draft, Visualization, Methodology, Formal analysis. Guangmin Ren: Writing – review & editing, Software, Resources, Project administration, Data curation. Qingjie Guo: Writing – review & editing, Resources, Funding acquisition. Hongjing Tian: Writing – review & editing, Supervision, Resources, Project administration, Methodology, Investigation, Funding acquisition, Conceptualization.

Declaration of Competing Interest

The authors declare that they have no known competing financial interests or personal relationships that could have appeared to influence the work reported in this paper.

Acknowledgements

This work was supported by National Natural Science Foundation of China (51106077) and Natural Science Foundation of Shandong Province (ZR2021MB118).

Supplementary Material

Supplementary data to this article can be found online at https://doi.org/10.1016/j.cjche.2026.01.011.

References

[1] W. Shi, J.Y. Li, F. Gao, L.J. Meng, X. Su, Z.W. Wang, Strongly coordinating mediator enables single-step resource recovery from heavy metal-organic complexes in wastewater, *Nat. Commun.* 15 (2024) 10828.
[2] U. Ghosh, A. Pal, Insight into the multiple roles of nitrogen doped carbon quantum dots in an ultrathin 2D-0D-2D all-solid-state Z scheme heterostructure and its performance in tetracycline degradation under LED illumination, *Chem. Eng. J.* 431 (2022) 133914.
[3] X.W. Zou, B. Sun, L. Wang, H.C. Bai, X.C. Meng, C.H. Li, Z.Z. Li, Enhanced photocatalytic degradation of tetracycline by SnS_2/Bi_2MoO_{6-x} heterojunction: multi-electric field modulation through oxygen vacancies and Z-scheme charge transfer, *Chem. Eng. J.* 482 (2024) 148818.
[4] H.R. Zhang, L. Zhang, S.S. Dong, X.G. Duan, D.Y. Zhu, B.J. Ni, C. Lyu, Regulating energy band structures of triazine covalent organic frameworks with

electron-donating/withdrawing substituents for visible-light-responsive photocatalytic tetracycline degradation and Cr(VI) reduction, *J. Hazard. Mater.* 446 (2023) 130756.
[5] J.T. Yang, F.Y. Chen, J. Hua, W.Q. Sun, Y.B. Tang, A new core-shell heterojunction MIL-53(Fe)@ZnIn2S4 for boosted photocatalytic degradation of tetracycline and reduction of Cr (VI) under visible irradiation, *Inorg. Chem. Commun.* 174 (2025) 114134.
[6] Y.H. Wen, Á. Rentería-Gómez, G.S. Day, M.F. Smith, T.H. Yan, R.O.K. Ozdemir, O. Gutierrez, V.K. Sharma, X.M. Ma, H.C. Zhou, Integrated photocatalytic reduction and oxidation of perfluorooctanoic acid by metal-organic frameworks: key insights into the degradation mechanisms, *J. Am. Chem. Soc.* 144 (26) (2022) 11840–11850.
[7] S.J. Li, X.Y. Li, Y.P. Liu, P. Zhang, J.L. Zhang, B. Zhang, Interfacial engineering of a plasmonic Ag/Ag_2CO_3/C_3N_5 S-scheme heterojunction for high-performance photocatalytic degradation of antibiotics, *Chin. J. Catal.* 72 (2025) 130–142.
[8] D.Y. Ma, Q.Q. Xue, Y.P. Liu, F.L. Liang, W.Y. Li, T. Liu, C.Q. Zhuang, Z.W. Zhao, S. J. Li, Manipulating interfacial charge redistribution in $Mn_{0.5}Cd_{0.5}S$/N-rich C_3N_5 S-scheme heterojunction for high-performance photocatalytic removal of emerging contaminants, *J. Mater. Sci. Technol.* 243 (2026) 265–274.
[9] J. Liu, Y.J. Xiang, Y.W. Chen, H.J. Zhang, B.J. Ye, L. Ren, W.F. Tan, A. Kappler, J.T. Hou, Quantitative contribution of oxygen vacancy defects to arsenate immobilization on hematite, *Environ. Sci. Technol.* 57 (33) (2023) 12453–12464.
[10] B. Liu, N.H. Zhou, J. Liu, X.L. Wang, P.K.J. Robertson, X.Y. Chen, C. Chen, J.M. Luo, C.Y. Wang, Full-spectrum Bi@$SrTiO_3$ for bi-directional promotion effects on photocatalytic redox reaction: insight into intermediates and mechanism, *J. Rare Earths* 42 (5) (2024) 917–925.
[11] N. Wang, H.T. Luo, L.L. Lu, P. Wu, G.D. Kang, J.Q. Chen, T. Xia, H. Zhou, S.H. Zhang, One-step calcination decomposition synthesis of $Bi_5O_7NO_3$/β-Bi_2O_3 for efficient degradation of norfloxacin: performance, mechanism and toxicity insights, *Chem. Eng. J.* 524 (2025) 169507.
[12] J.C. Xu, X.D. Zhang, X.F. Wang, X.H. Wu, H.G. Yu, Charge self-regulation over in-plane two-dimensional/two-dimensional hetero-cocatalyst for robust photocatalytic hydrogen generation, *J. Colloid Interface Sci.* 675 (2024) 592–601.
[13] J.C. Sin, S.M. Lam, H.H. Zeng, H. Lin, H.X. Li, L.L. Huang, S.J. Liaw, A.R. Mohamed, J.W. Lim, Integrating $BaFe_2O_4$ nanoparticles onto N-doped Bi_2WO_6 microspheres for eminent visible light-driven photocatalytic performance towards aquaculture contaminants and pathogens, *Colloids Surf. A Physicochem. Eng. Aspects* 692 (2024) 133905.
[14] D.Y. Li, S. Hussain, Y.J. Wang, C. Huang, P. Li, M.Y. Wang, T. He, ZnSe/CdSe Z-scheme composites with Se vacancy for efficient photocatalytic CO_2 reduction, *Appl. Catal. B Environ.* 286 (2021) 119887.
[15] Y. Lu, Y.L. Yang, X.Y. Fan, Y.Q. Li, D.H. Zhou, B. Cai, L.Y. Wang, K. Fan, K. Zhang, Boosting charge transport in BiVO(4) photoanode for solar water oxidation, *Adv. Mater.* 34 (8) (2022) e2108178.
[16] W.T. Song, K.C. Chong, G.B. Qi, Y.K. Xiao, G.W. Chen, B.W. Li, Y.F. Tang, X.Y. Zhang, Y.F. Yao, Z.Q. Lin, Z.G. Zou, B. Liu, Unraveling the transformation from type-II to Z-scheme in perovskite-based heterostructures for enhanced photocatalytic CO_2 reduction, *J. Am. Chem. Soc.* 146 (5) (2024) 3303–3314.
[17] S.J. Li, Y.Q. Zhao, X.L. Zhang, Y.P. Liu, T. Liu, W.Y. Li, Y.P. Hou, W. Jiang, B. Zhang, Floatable S-scheme $Bi_4O_5Br_2$/C_3N_4/carbon fiber cloth with robust internal electric field for efficient photocatalytic antibiotic decontamination, *Adv. Fiber Mater.* 7 (6) (2025) 2032–2047.
[18] S.J. Li, R. Li, K.X. Dong, Y.P. Liu, X. Yu, W.Y. Li, T. Liu, Z.W. Zhao, M.Y. Zhang, B. Zhang, X.B. Chen, Self-floating $Bi_4O_5Br_2$/P-doped C_3N_4/carbon fiber cloth with S-scheme heterostructure for boosted photocatalytic removal of emerging organic contaminants, *Chin. J. Catal.* 76 (2025) 37–49.
[19] Z.S. Chen, J.Y. Wang, M.J. Hao, Y.H. Xie, X.L. Liu, H. Yang, G.I.N. Waterhouse, X. K. Wang, S.Q. Ma, Tuning excited state electronic structure and charge transport in covalent organic frameworks for enhanced photocatalytic performance, *Nat. Commun.* 14 (1) (2023) 1106.
[20] Y.X. He, J. Qian, P.F. Wang, T.P. Xie, D.D. Dionysiou, B.H. Lu, S.J. Tang, Synergized selenium-vacancy heterogeneous interface and carbon nanotubes for insight into efficient oxidation of pollutants *via* photocatalytic peroxymonosulfate activation, *Appl. Catal. B Environ.* 330 (2023) 122620.
[21] B. Shen, H. Du, A.X. Liu, N.Y. Li, C. Chen, L.G. Shen, Y.X. Hui, R.B. Huo, Z. Zhang, Q. Wang, Interfacial electric field steering S-scheme charge transfer in MIL-88A(Fe)/polydopamine heterojunctions: dual-redox pathways for efficient pollutant mineralization, *J. Clean. Prod.* 523 (2025) 146458.
[22] Y. Liu, H.T.D. Bui, A.R. Jadhav, T. Yang, S. Saqlain, Y.G. Luo, J.M. Yu, A. Kumar, H.D. Wang, L.L. Wang, V.Q. Bui, M.G. Kim, Y.D. Kim, H. Lee, Revealing the synergy of cation and anion vacancies on improving overall water splitting kinetics, *Adv. Funct. Mater.* 31 (21) (2021) 2010718.
[23] J. Zhang, D.S. Yang, Z. Yang, L.L. Wang, Utilizing cationic vacancy defects to switch oxygen evolution mechanisms on atomically dispersed ru for enhanced acidic catalytic performance, *Appl. Catal. B Environ. Energy* 364 (2025) 124845.
[24] J.H. Zhao, Y.F. Wang, H. Liu, R. Zhang, W.L. Jia, J.H. Zhang, Y. Sun, L.C. Peng, Understanding the role of dual zinc and indium vacancies in $ZnIn_2S_4$ for the visible-light-driven photocatalytic air-oxidation of 5-hydroxymethylfurfural, *ACS Catal.* 15 (4) (2025) 3464–3474.
[25] H.J. Chen, R.H. Xu, D. Chen, T.L. Lu, H.J. Li, M. Wang, Subsurface Mo vacancy in bismuth molybdate promotes photocatalytic oxidation of lactate to pyruvate, *ACS Catal.* 14 (3) (2024) 1977–1986.
[26] J.T. Huang, T. Lin, L.Y. Lin, G.J. Ma, Z.Y. Zhang, S. Handschuh-Wang, A.Y. Meng, P.G. Han, B. He, Boosted charge transport efficiency for bismuth and oxygen dual vacancy-engineered $BiVO_4$ photoanodes, *ACS Appl. Energy Mater.* 7 (22) (2024) 10710–10720.
[27] L. Wang, Y.K. Li, Y.Y. Ai, E.C. Fan, F. Zhang, W.T. Zhang, G.S. Shao, P. Zhang, Tracking heterogeneous interface charge reverse separation in $SrTiO_3$/NiO/NiS nanofibers with *in situ* irradiation XPS, *Adv. Funct. Mater.* 33 (44) (2023) 2306466.
[28] L. Yang, X.X. Jiang, X.M. Jin, J.R. Zhang, R.Z. Li, Y. Luo, H.Y. Li, Yeast-templated *in situ* hydrothermal synthesis of carbon modified Bi_2MoO_6/Bi_2S_3 microspheres with efficient photocatalytic performance, *Ceram. Int.* 50 (21) (2024) 42632–42644.
[29] X.J. Yang, X.J. Li, B. Zhang, T.F. Liu, Z.P. Chen, Oxygen vacancies enriched hollow Bi_2MoO_6 microspheres for efficient photocatalytic oxidation of hydrocarbons, *ACS Sustainable Chem. Eng.* 12 (17) (2024) 6519–6528.
[30] M.Y. Wang, H. Yu, N. Yang, K. Yu, Ferroelectric polarization-electric field promoted S-scheme CdSe/Ba_xSr_{1-x}TiO3 for highly efficient solar hydrogen evolution, *Sep. Purif. Technol.* 354 (2025) 128919.
[31] H. Wang, P.Y. Yang, W.J. Zhao, S.H. Ma, J.H. Hou, Q.F. He, C.L. Wu, H.A. Chen, Q. Wang, Q. Cheng, B.S. Guo, J.C. Qiao, W.J. Lu, S.J. Zhao, X.D. Xu, C.T. Liu, Y. Liu, C.W. Pao, Y. Yang, Lattice distortion enabling enhanced strength and plasticity in high entropy intermetallic alloy, *Nat. Commun.* 15 (1) (2024) 6782.
[32] S.B. Cao, Y.W. Zeng, Y. Li, K. Da, W.T. Chen, J. Yang, X.M. Fan, The presence of Mo and O double vacancies in $Bi_2W_{0.25}Mo_{0.75}O_6$ solid solution promotes photogenerated charge separation and molecular oxygen activation for efficient removal of gaseous toluene under visible light, *Sep. Purif. Technol.* 354 (2025) 128958.
[33] A.Q. Wang, Y.K. Wen, H.D. Zhu, Z. Liu, H. Wang, W.N. Yao, Y.L. Fan, G.C. Xie, X. H. Chen, K. Yan, Q. Duan, Z.W. Jiang, M.M. Xu, Y.D. Wei, H. Lin, Oxygen vacancy mediated photocatalysis of Ti3C2 MXene quantum dots/$W_{18}O_{49}$ hybrid membrane for peroxymonosulfate-enhanced oxidation degradation, *Chem. Eng. J.* 496 (2024) 154264.
[34] L.Q. Zhang, Z.L. Jin, *In situ* proof construction of GDY/$NiWO_4$/CdS double S-scheme heterojunction: improving charge transfer and promoting photocatalytic activity, *Chem. Eng. J.* 497 (2024) 154548.
[35] R.Y. Zeng, C.C. Cheng, F.S. Xing, Y. Zou, K.N. Ding, C.J. Huang, Dual vacancies induced local polarization electric field for high-performance photocatalytic H_2 production, *Appl. Catal. B Environ.* 316 (2022) 121680.
[36] C.L. Li, Y.F. Wang, S.R. Chen, W. Zhang, Z. Wang, Z.Y. Hou, Enhanced photoelectrochemical performance based on conformal and uniform ZnO/ZnSe/CdSe heterostructures on Zn foil substrate, *Int. J. Hydrogen Energy* 45 (15) (2020) 8257–8272.
[37] M.W. Liu, W.H. Yang, R.S. Xiao, Y. Qin, R. Tan, Y.X. Chen, W.L. Gu, L.Y. Hu, Y.H. Lin, C.Z. Zhu, Anisotropic dual S-scheme heterojunctions mimic natural photosynthetic system for boosting photoelectric response, *Angew. Chem. Int. Ed.* 63 (33) (2024) e202407481.
[38] H.W. Zhu, H.F. Shi, J.P. Li, X.S. Qu, S.S. Zhao, H.S. Wang, A. Rong, Z. Chen, Construction of S-scheme $Cs_3PMo_{12}O_{40}$/$MnIn_2S_4$ heterojunction for efficient photocatalytic removal of antibiotics: degradation pathways, toxicity evaluation and mechanism insight, *J. Alloys Compd.* 976 (2024) 173072.
[39] Y.S. Li, D.M. Han, Z.H. Wang, F.B. Gu, Double-solvent-induced derivatization of Bi-MOF to vacancy-rich $Bi_4O_5Br_2$: toward efficient photocatalytic degradation of ciprofloxacin in water and HCHO gas, *ACS Appl. Mater. Interfaces* 16 (6) (2024) 7080–7096.
[40] Y. Fang, Y. Cao, B.H. Tan, Q.L. Chen, Oxygen and titanium vacancies in a BiOBr/MXene-Ti_3C_2 composite for boosting photocatalytic N_2 fixation, *ACS Appl. Mater. Interfaces* 13 (36) (2021) 42624–42634.
[41] X. Shi, W.D. Dai, X.A. Dong, Q. Ren, J.P. Sheng, F. Dong, Dual Cu and S vacancies boost CO_2 photomethanation on $Cu_{1.95}S_{1-x}$: Vacancy-regulated selective photocatalysis, *Appl. Catal. B Environ.* 339 (2023) 123147.
[42] W. Li, Z.L. Liu, Y.B. Dong, L.Q. Wang, Z. Liu, L. Zhang, Z.N. Qiao, Micellar interface modulation self-assembly strategy towards mesoporous bismuth oxychloride-based materials for boosting photocatalytic pharmaceuticals degradation, *Chem. Eng. J.* 450 (2022) 137897.
[43] S.J. Li, C.J. You, K. Rong, C.Q. Zhuang, X.B. Chen, B. Zhang, Chemically bonded $Mn_{0.5}Cd_{0.5}S$/BiOBr S-scheme photocatalyst with rich oxygen vacancies for improved photocatalytic decontamination performance, *Adv. Powder Mater.* 3 (3) (2024) 100183.
[44] A. Verma, S. Kumar, Y.P. Fu, A ternary-hybrid as efficiently photocatalytic antibiotic degradation and electrochemical pollutant detection, *Chem. Eng. J.* 408 (2021) 127290.
[45] D.C. Jiang, S.N. Hu, Y. Qu, X. Tian, H.W. Du, C.H. Zhu, Z.J. Li, L.S. Yin, Y.P. Yuan, G. Liu, Infrared irradiation-lattice vibration coupling-initiated N→Π* electronic transition in carbon nitride nanosheets for increased photocatalysis, *Adv. Funct. Mater.* 34 (16) (2024) 2311803.
[46] L.M. Jin, M. Deng, J. Gao, L.C. Wang, Q. Zhou, X.J. Tang, Q. Li, H. Du, D. Hao, Q. Wang, A crystalline triazine covalent organic framework with partial fluorination for efficient hydrogen peroxide production toward water treatment, *Chem. Eng. J.* 515 (2025) 163722.
[47] Y.X. Li, W.L. Su, Y.S. Yang, L.X. Bai, J. Lu, W.K. Zhang, S. Wei, *In situ* topotactic formation of the pn-type inorganic intergrowth bulk heterojunction NiO(Al)/CuO(Ni, Al) for photocatalytic CO_2 methanation, *Appl. Catal. B Environ.* 341 (2024) 123282.

[48] X.N. Tong, J.X. Shou, H. Song, Y.L. Wang, L. Huang, L.S. Yin, Ultrafast electron transfer from crystalline g-C_3N_4 to Pt revealed by femtosecond transient absorption spectroscopy, *Energy Fuel.* 36 (19) (2022) 11532−11541.
[49] C. Cheng, J.J. Zhang, B.C. Zhu, G.J. Liang, L.Y. Zhang, J.G. Yu, Verifying the charge-transfer mechanism in S-scheme heterojunctions using femtosecond transient absorption spectroscopy, *Angew. Chem. Int. Ed.* 62 (8) (2023) e202218688.
[50] P.Y. Dong, K.J. Gao, L.H. Zhang, H.K. Huan, M.H. Xie, X.L. Yang, J.L. Zhang, Hydrogen bond-assisted construction of MOF/semiconductor heterojunction photocatalysts for highly efficient electron transfer, *Appl. Catal. B Environ. Energy* 357 (2024) 124297.
[51] T.J. Ma, H.Y. Long, Z.H. Shi, Z.C. Lang, M.X. Zhao, S.Q. Zhang, C.S. Lei, Efficient photocatalytic degradation of TC under visible light with three-dimensional flower shaped N doped BiOBr/$CuBi_2O_4$, *Opt. Mater.* 143 (2023) 114175.
[52] C.C. Wang, S.J. Li, M.J. Cai, R.Y. Yan, K.X. Dong, J.L. Zhang, Y.P. Liu, Rationally designed tetra (4-carboxyphenyl) porphyrin/graphene quantum dots/bismuth molybdate Z-scheme heterojunction for tetracycline degradation and Cr(VI) reduction: performance, mechanism, intermediate toxicity appraisement, *J. Colloid Interface Sci.* 619 (2022) 307−321.
[53] S.J. Li, M.J. Cai, C.C. Wang, Y.P. Liu, N. Li, P. Zhang, X. Li, Rationally designed Ta3N5/BiOCl S-scheme heterojunction with oxygen vacancies for elimination of tetracycline antibiotic and Cr(VI): performance, toxicity evaluation and mechanism insight, *J. Mater. Sci. Technol.* 123 (2022) 177−190.
[54] X.T. Kong, J.X. Ma, S. Garg, T.D. Waite, Tailored metal-organic frameworks for water purification: perfluorinated Fe-MOFs for enhanced heterogeneous catalytic ozonation, *Environ. Sci. Technol.* 58 (20) (2024) 8988−8999.
[55] P. Zhang, N. Xiao, L. Yang, S.L. Liu, J.K. Wang, J.Y. Hu, Z.B. Tong, G.Q. Zhang, S. M. Ding, Y.Q. Yu, Active species trapping test for the mechanism study of photocatalytic dye degradation: a critical examination, *Appl. Catal. A-Gen.* 707 (2025) 120527. https://doi.org/10.1016/j.apcata.2025.120527.
[56] J.B. Lin, B. He, X. Li, X.H. Wang, L.Z. Zhang, P.J.J. Alvarez, M.C. Long, *In-situ* formed Zr-phosphonate surface complex promotes peroxymonosulfate activation of single-atom Cu for efficient phosphonate oxidation, *Environ. Sci. Technol.* 59 (29) (2025) 15547−15557.